

Scale-invariant patterning by size-dependent inhibition of Nodal signalling

María Almuedo-Castillo^{1,3}, Alexander Bläßle¹, David Mörsdorf¹, Luciano Marcon^{1,3}, Gary H. Soh¹, Katherine W. Rogers^{1,2}, Alexander F. Schier² and Patrick Müller^{1*}

Individuals can vary substantially in size, but the proportions of their body plans are often maintained. We generated smaller zebrafish by removing 30% of their cells at the blastula stages and found that these embryos developed into normally patterned individuals. Strikingly, the proportions of all germ layers adjusted to the new embryo size within 2 hours after cell removal. As Nodal–Lefty signalling controls germ-layer patterning, we performed a computational screen for scale-invariant models of this activator–inhibitor system. This analysis predicted that the concentration of the highly diffusive inhibitor Lefty increases in smaller embryos, leading to a decreased Nodal activity range and contracted germ-layer dimensions. In vivo studies confirmed that Lefty concentration increased in smaller embryos, and embryos with reduced Lefty levels or with diffusion-hindered Lefty failed to scale their tissue proportions. These results reveal that size-dependent inhibition of Nodal signalling allows scale-invariant patterning.

Despite often substantial variability in size, embryos faithfully generate the correct tissue proportions^{1–5}. During development, tissue patterning is achieved by gradients of signalling proteins that induce distinct differentiation programmes in discrete spatial domains^{6–10}. To adjust tissue patterning and organ proportions to their body size, embryos need to appropriately scale the underlying signalling gradients¹¹. Scaling mechanisms for individual tissue-specific signalling systems at different stages of development have been proposed, but how these mechanisms are integrated and coordinated during development to generate the correct proportions of all tissues is currently unclear^{11–21}. Here, we analysed how signalling gradients adjust tissue proportions in differently sized zebrafish embryos and identified a size-dependent mechanism that mediates scale-invariant germ-layer patterning to provide the correct amount of progenitor cells for all future tissues.

Results

Scaling of tissue proportions in differently sized zebrafish embryos. We found that the removal of ~30% of cells by extirpation from the animal pole before gastrulation (Fig. 1a) generates zebrafish embryos that become normally patterned adults. Extirpated embryos developed into smaller individuals with the same number of proportionally thinner somites as untreated embryos (Fig. 1a). Consistently, the size of various organs, including the hatching gland (a mesodermal derivative, *hgg1* positive) and the eye (an ectodermal derivative, *vsx2* positive), was reduced in individuals developing from extirpated embryos (Fig. 1b). Strikingly, scaling of tissue proportions to embryo size already occurred during the gastrulation stages within 2 hours following extirpation. Using in situ hybridization, we quantified the extent of the presumptive ectoderm (*sox3* positive; Fig. 1c) and mesendoderm (*fascin* positive; Fig. 1d) and found that the germ-layer proportions adjusted progressively after extirpation: at 1-hour post-extirpation (1 hpe), extirpated embryos had excess mesendoderm and insufficient ectodermal progenitors as cells were removed from the animal pole

containing presumptive ectoderm (Fig. 1c,d). Interestingly, 1 hour later (2 hpe), the ectoderm and mesendoderm proportions had adjusted in extirpated embryos (Fig. 1c,d). Using in toto light-sheet imaging, we confirmed that the mesendoderm scaled throughout the embryonic marginal zone (Fig. 1e–g). Even though cells were removed from the animal pole, the number of endodermal precursor cells (*sox17* and *sox32* positive) at the opposite side within the marginal zone of extirpated embryos was also proportionally reduced by the gastrulation stages (Fig. 1h).

Smaller embryos do not adjust developmental speed after extirpation. The cell density did not change (Fig. 2a) and the proliferation rates did not increase in extirpated embryos (Fig. 2b,c), indicating that neither changes in cell density nor compensatory proliferation underlie germ-layer scaling. Moreover, the spatial expression kinetics of *gooseoid*²²—a highly sensitive indicator of developmental progression—were similar in untreated and extirpated embryos at different developmental time points (Supplementary Fig. 1). Even though smaller embryos displayed a reduced apparent epiboly due to the shortened blastoderm but unchanged yolk extent after extirpation, the spreading of the blastoderm during epiboly occurred at a similar pace (Fig. 2d–i). Thus, scaling can also not be explained by altered developmental speed in differently sized embryos.

Nodal signalling scales in smaller embryos. As the Nodal–Lefty activator–inhibitor system patterns the germ layers during early development^{10,23}, we hypothesized that Nodal signalling adjusts in smaller embryos to allow proportionate patterning. The activator Nodal is secreted from the marginal zone of the embryo and induces the endoderm and mesoderm, whereas the highly diffusive Nodal inhibitor Lefty²⁴, which is also expressed at the margin and induced by Nodal signalling, limits the mesendodermal domain^{23,25–34}. To test whether Nodal signalling adjusts in smaller embryos, we measured the extent of Nodal activity by assessing the phosphorylation of the Nodal signal transducer Smad2/3 (pSmad2/3)^{23,35,36} (Fig. 3a–d and

¹Friedrich Miescher Laboratory of the Max Planck Society, Tübingen, Germany. ²Department of Molecular and Cellular Biology, Harvard University, Cambridge, MA, USA. ³Present address: Centro Andaluz de Biología del Desarrollo, Universidad Pablo de Olavide, Sevilla, Spain.

*e-mail: patrick.mueller@tuebingen.mpg.de

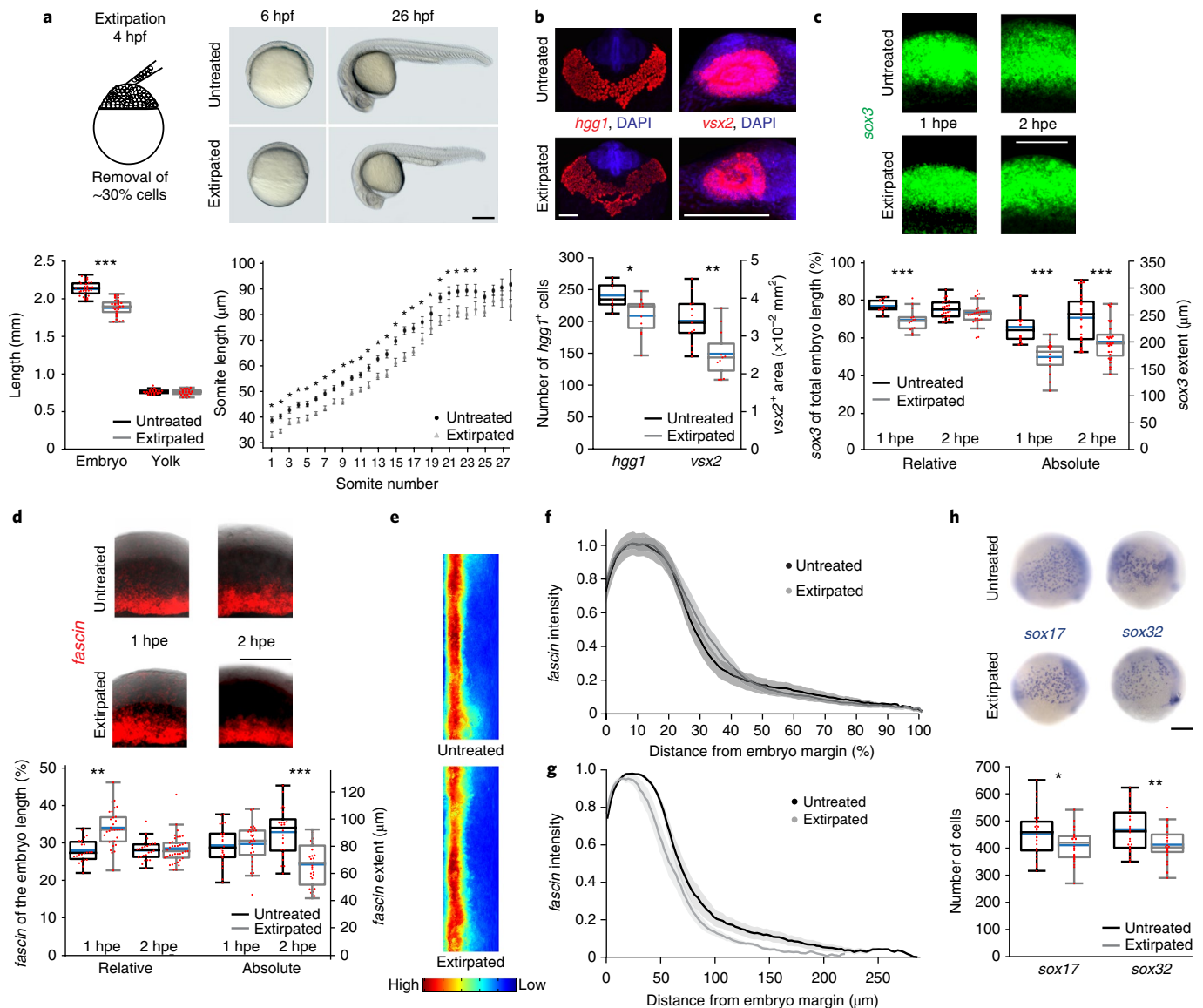


Fig. 1 | Scaling in smaller embryos after extirpation. **a**, Schematic of embryo extirpation (lateral views); hpf, hours post-fertilization. The total length of extirpated embryos at 1-day post-fertilization is smaller than untreated individuals (n of untreated = 40, n of extirpated = 37; $***P < 0.00001$), whereas the yolk size remains unchanged (n of untreated = 23, n of extirpated = 24; $P > 0.05$) (bottom left). The length of the 24 posterior-most somites is proportionately smaller in extirpated embryos (bottom right, n of untreated = 15, n of extirpated = 13; $*P < 0.05$). The error bars in the ‘Somite length’ graph are the s.e.m. **b**, Maximum intensity projections of confocal FISH stacks (top) and the quantification of *hgg1*-positive cells (n of untreated = 9, n of extirpated = 11; $*P < 0.05$) and *vsx2*-positive cells (n of untreated = 13, n of extirpated = 11; $**P < 0.01$) (bottom). **c,d**, Maximum intensity projections of lateral confocal FISH stacks (top) and the quantification of the relative and absolute length of *sox3* (ectoderm; **c**) and *fascin* (mesendoderm; **d**) domains (bottom). The ectoderm proportions are smaller at 1 hpe (n of untreated = 14, n of extirpated = 14; $***P < 0.001$) but scale by 2 hpe (n of untreated = 28, n of extirpated = 28; $P > 0.05$). Similarly, the mesendoderm proportions are too large at 1 hpe (n of untreated = 23, n of extirpated = 31; $**P < 0.01$) but scale by 2 hpe (n of untreated = 24, n of extirpated = 37; $P > 0.05$). **e-g**, 2D maps of 3D-reconstructed embryos imaged by light-sheet microscopy (**e**) and the quantification (**f,g**) of normalized *fascin* domains along the vegetal-animal axis show scaling (n of untreated = 9, n of extirpated = 9). The shaded regions in **f** and **g** are the s.e.m. **h**, Lateral views and the quantification of the number of endodermal cells positive for *sox17* (n of untreated = 30, n of extirpated = 27; $*P < 0.05$) or *sox32* (n of untreated = 26, n of extirpated = 28; $**P < 0.01$). The box plots show the median (blue line), the mean (black (untreated) and grey (extirpated) lines inside the box), the 25% and 75% quantiles (box) and all included data points (red markers). Whiskers extend to the smallest data point within the 1.5 interquartile range of the lower quartile and to the largest data point within the 1.5 interquartile range of the upper quartile. Two-sided Student’s *t*-tests were performed ($\alpha = 0.05$). See Supplementary Table 1 for statistics source data. Scale bars, 200 μm.

Supplementary Fig. 2a,b). Similar to the mesendodermal domain (Fig. 1e,f), Nodal signalling scaled throughout the embryonic marginal zone by 2 hpe (Fig. 3b,c). Interestingly, Nodal signalling had already scaled by 1 hpe (Fig. 3a and Supplementary Fig. 2a,b), preceding the scaling of the presumptive ectoderm/mesendoderm

(Fig. 1c,d) and the feedback-induced Nodals (*cyclops* and *squint*) and Leftys (*lefty1* (*lft1*) and *lefty2* (*lft2*)) (Fig. 3e–i).

A computational screen to identify scaling mechanisms. To identify the mechanism by which Nodal signalling might sense embryo size

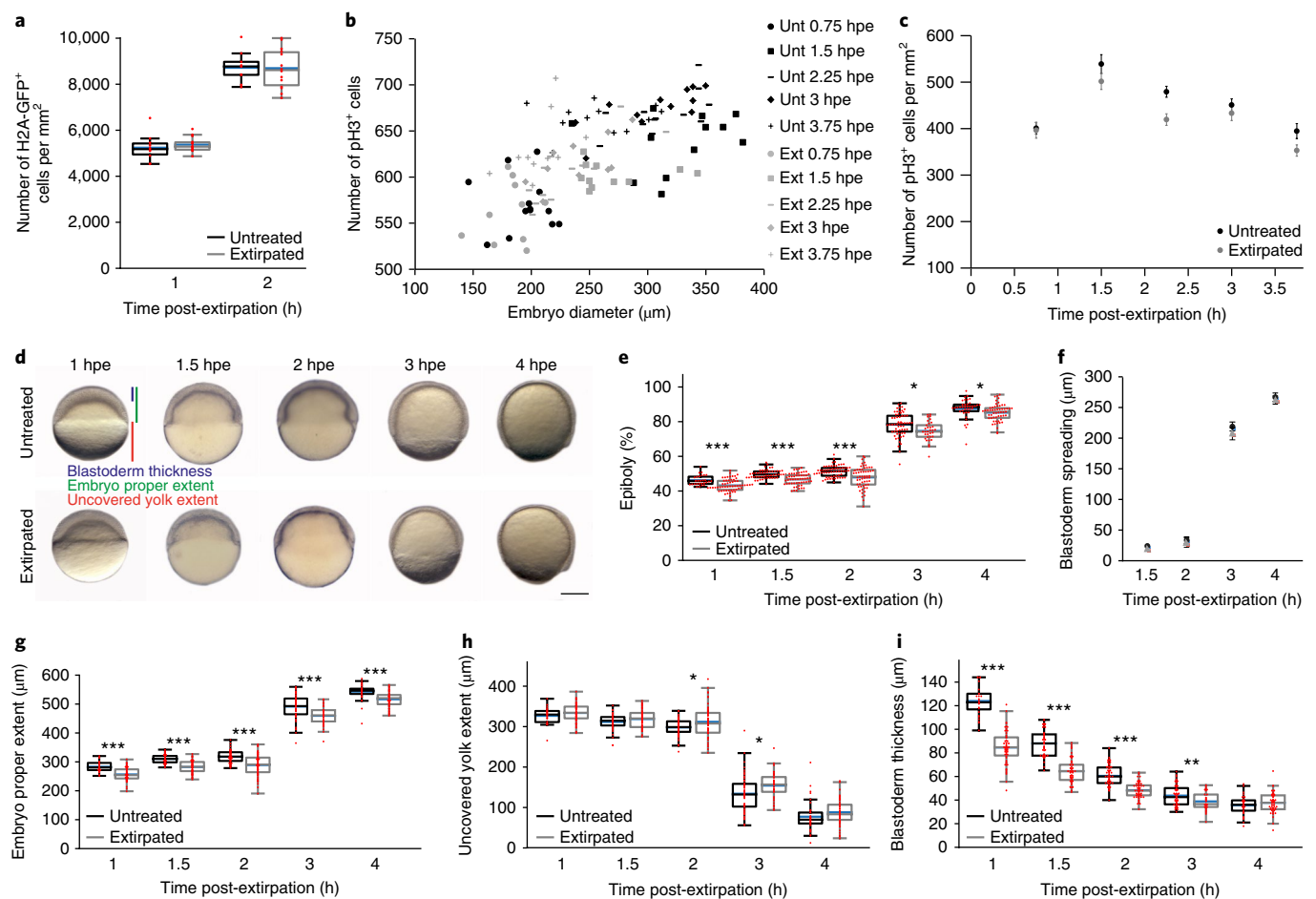


Fig. 2 | Germ-layer proportions scale in extirpated embryos without increases in cell proliferation or changes in cell density or developmental speed. **a**, Cell density measured in untreated and extirpated H2A-GFP embryos at different time points after extirpation. 1 hpe: n of untreated = 10, n of extirpated = 14, $P > 0.05$; 2 hpe: n of untreated = 9, n of extirpated = 14; $P > 0.05$. **b,c**, The number of proliferating cells (pH3 positive) relative to the embryo diameter (**b**) and the density of proliferating cells (**c**) in untreated (Unt) and extirpated (Ext) embryos at different time points after extirpation. 0.75 hpe: n of untreated = 13, n of extirpated = 11, $P > 0.05$; 1.5 hpe: n of untreated = 12, n of extirpated = 11, $P > 0.05$; 2.25 hpe: n of untreated = 12, n of extirpated = 12, $**P < 0.01$; 3 hpe: n of untreated = 12, n of extirpated = 10, $P > 0.05$; 3.75 hpe: n of untreated = 12, n of extirpated = 11, $P > 0.05$. Individual data points are shown in **b**; the mean and s.e.m. of the same data are shown in **c**. **d**, Lateral views of untreated and extirpated embryos. The progression of gastrulation and epiboly spreading is unchanged after extirpation. Scale bar, 200 μm . **e-i**, Quantification of the epiboly (%) (that is, the ratio of the embryo proper extent to the total length (embryo proper + uncovered yolk) (**e**), blastoderm spreading (that is, the difference between the embryo proper extent at 1.5, 2, 3 and 4 hpe and the embryo proper extent at the first time point of analysis (1 hpe) (**f**), the extent of the embryo proper (**g**), the uncovered yolk (**h**) and the blastoderm thickness (**i**) at different time points after extirpation. 1 hpe: n of untreated = 28, n of extirpated = 59; 1.5 hpe: n of untreated = 51, n of extirpated = 55; 2 hpe: n of untreated = 62, n of extirpated = 58; 3 hpe: n of untreated = 59, n of extirpated = 33; 4 hpe: n of untreated = 38, n of extirpated = 55. $*P < 0.05$; $**P < 0.01$; $***P < 0.001$. The mean and s.e.m. are shown in **f**. The box plots show the median (blue line), the mean (black (untreated) and grey (extirpated) lines), 25% and 75% quantiles (box) and all included data points (red markers). Whiskers extend to the smallest data point within the 1.5 interquartile range of the lower quartile and to the largest data point within the 1.5 interquartile range of the upper quartile. Two-sided Student's t -tests were performed ($\alpha = 0.05$). See Supplementary Table 1 for statistics source data.

and adjust tissue proportions, we performed a computational screen that included known positive and negative interactions in the Nodal–Lefty system^{23,33,34} while keeping model complexity to a minimum (Fig. 4a,b and Supplementary Note 1). We constrained the screen with the measured biophysical properties, including Nodal/Lefty diffusivities and half-lives³³, and systematically varied the unknown parameters to identify systems that recapitulate the scaling observed during germ-layer patterning. To keep model complexity to a minimum, we did not account for spatial biases influencing the Nodal–Lefty system³⁷ and did not explicitly model receptor interactions³⁸.

We screened more than 400,000 parameter combinations representing the production of Lefty, the inhibition strength and the Nodal-mediated feedback on Nodal and Lefty production. By assessing the overlap between Nodal signalling in simulations

of normally sized and shortened embryos, we found that systems that are capable of scaling require precise levels of highly diffusive Lefty, whose concentration increases in extirpated embryos to adjust the Nodal signalling gradient (Fig. 4c–e). In such systems, the boundary located more proximal to the marginal zone in shortened compared to normally sized embryos affects the long-range Lefty but not the short-range Nodal gradient (Fig. 4c). As we shortened embryos before the onset of Lefty protein secretion without removing *lft*-expressing cells from the marginal zone (Fig. 3e–i), the same amount of Lefty should be produced in early extirpated and untreated embryos. Thus, the concentration of Lefty should increase in smaller embryos, contracting the Nodal activity range to re-establish the correct tissue dimensions relative to the new size of the embryo.

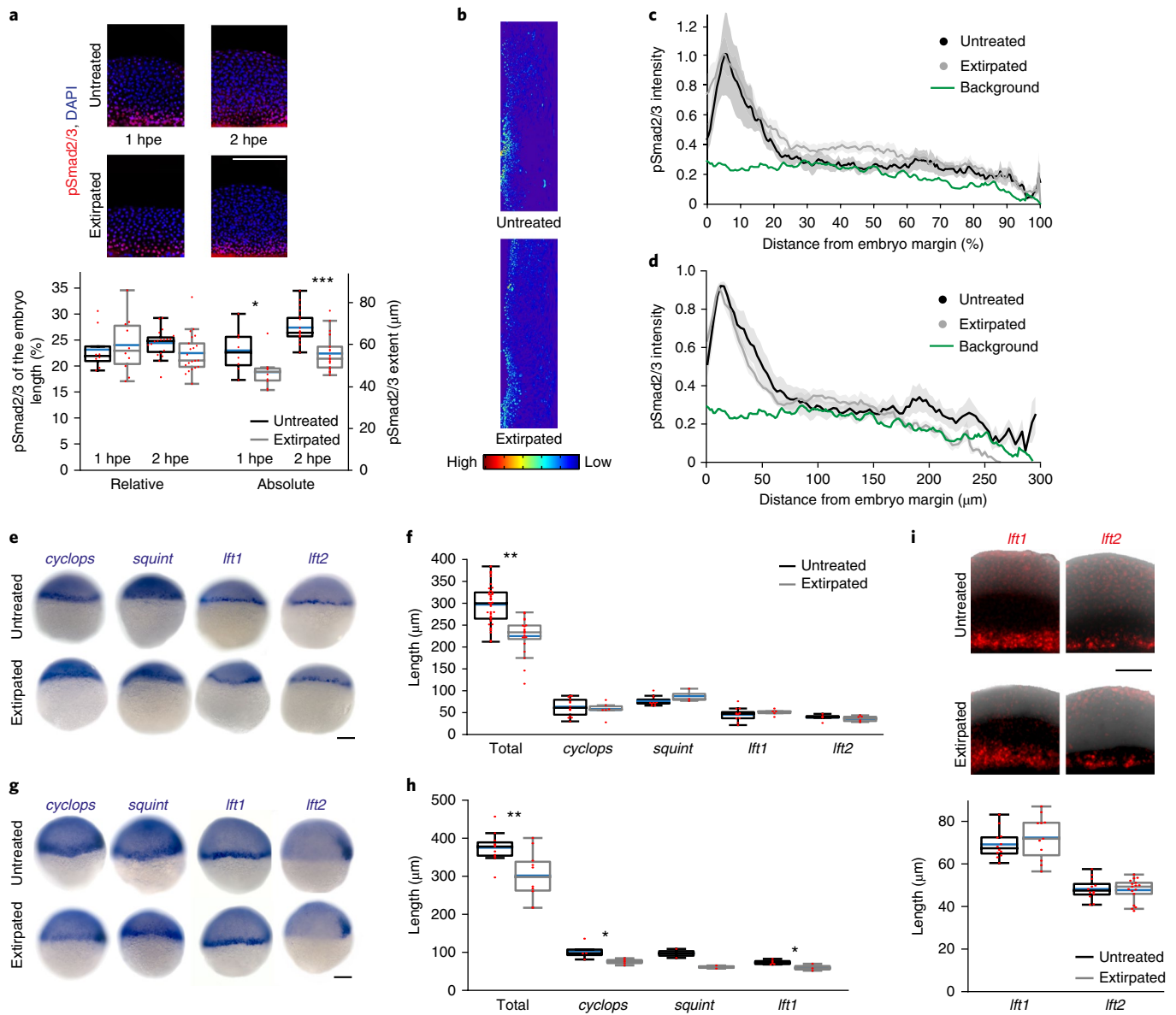


Fig. 3 | Scaling of Nodal-mediated patterning. **a**, Maximum intensity projections of lateral confocal pSmad2/3 immunostaining stacks (top) and the quantification of the absolute and relative length of the pSmad2/3 domain (bottom). 1 hpe: n of untreated = 7, n of extirpated = 10; 2 hpe: n of untreated = 19, n of extirpated = 21. **b-d**, 2D maps of 3D-reconstructed embryos imaged by light-sheet microscopy (**b**) and the quantification of normalized pSmad2/3 domains along the vegetal-animal axis show scaling (n of untreated = 5, n of extirpated = 6). Intensity as a function of embryo length (%) (**c**) and intensity as a function of the absolute distance from the margin (**d**) are shown. The shaded regions in **c** and **d** are the s.e.m. **e-h**, Lateral images showing the expression of *cyclops* and *squint* Nodals and *lft1* and *lft2* Leftys in untreated and extirpated embryos at 1 hpe (**e**) and 2 hpe (**g**), and the quantification of embryo length and expression domains at 1 hpe (**f**) and 2 hpe (**h**). 1 hpe: total: n of untreated = 42, n of extirpated = 20; *cyclops*: n of untreated = 14, n of extirpated = 6; *squint*: n of untreated = 11, n of extirpated = 3; *lft1*: n of untreated = 12, n of extirpated = 5; *lft2*: n of untreated = 5, n of extirpated = 6. 2 hpe: total: n of untreated = 11, n of extirpated = 10; *cyclops*: n of untreated = 4, n of extirpated = 5; *squint*: n of untreated = 2, n of extirpated = 2; *lft1*: n of untreated = 5, n of extirpated = 3. Nodal and Lefty domains are unchanged in differently sized embryos at 1 hpe but scale by 2 hpe. **i**, Maximum intensity projections of lateral confocal *lft1* and *lft2* FISH stacks in untreated and extirpated embryos at 1 hpe (top) and the quantification of expression domains (bottom). *lft1*: n of untreated = 12, n of extirpated = 11; *lft2*: n of untreated = 12, n of extirpated = 17. The box plots show the median (blue line), the mean (black (untreated) and grey (extirpated) lines), 25% and 75% quantiles (box) and all included data points (red markers). Whiskers extend to the smallest data point within the 1.5 interquartile range of the lower quartile and to the largest data point within the 1.5 interquartile range of the upper quartile. Two-sided Student's *t*-tests were performed ($\alpha = 0.05$). * $P < 0.05$; ** $P < 0.01$; *** $P < 0.001$. See Supplementary Table 1 for statistics source data. Scale bars, 200 μm (**a,e,g**) and 100 μm (**i**).

In our simulations of the Nodal–Lefty system (Supplementary Video 1), scale-invariant germ-layer patterning only became apparent around 2 hpe, as observed experimentally (Fig. 1c,d). The simulations further closely matched the time window of germ-layer specification: Nodal signalling levels and mesendoderm

specification expand as development proceeds, Nodal signalling levels peak around 2 hpe (6 hours post-fertilization (6hpf)) and Nodal signalling rapidly decreases afterwards (Supplementary Video 1). Together, the experimental observations and computational simulations suggest that germ-layer scaling at 2 hpe results from

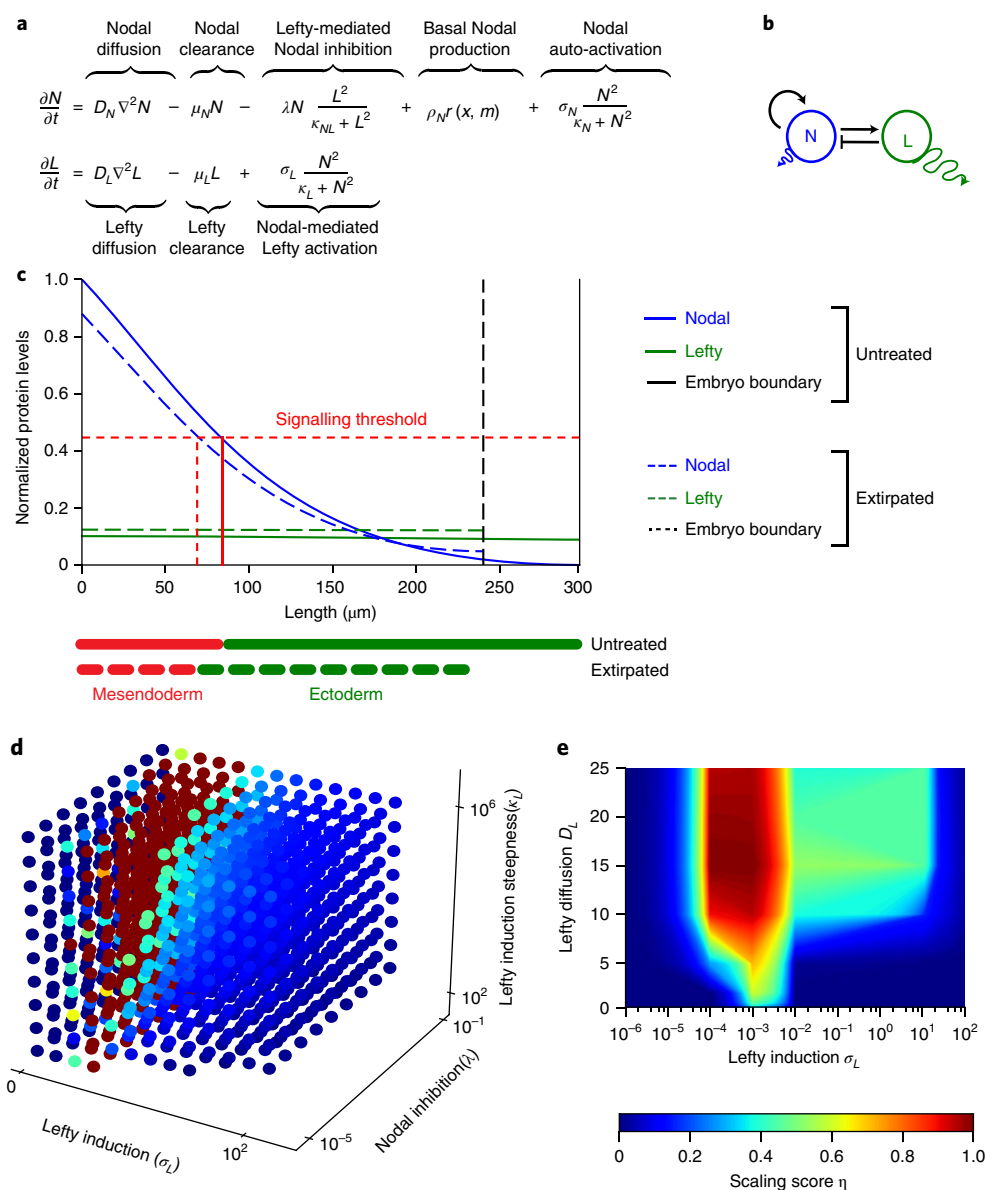


Fig. 4 | Computational screen for parameters conferring scale invariance. **a, b**, Equations (**a**) and network (**b**) describing the known interactions in the Nodal (N)–Lefty (L) activator–inhibitor system. The change in Nodal concentration over time (t) is a function of Nodal diffusion with the diffusion coefficient D_N , Nodal removal with the clearance rate constant μ_N , Lefty-mediated Nodal inhibition with the inhibition strength λ and the steepness parameter κ_{NL} , basal Nodal production described by the space (x)–dependent rectangular pulse function $r(x, m)$ representing the length m of the Nodal source, and Nodal auto-activation with the rate constant σ_N and the steepness parameter κ_N . Similarly, the change in Lefty concentration over time is a function of Lefty diffusion with the diffusion coefficient D_L , Lefty removal with the clearance rate constant μ_L , and Nodal-dependent Lefty induction with the rate constant σ_L and the steepness parameter κ_L . **c**, Example of a scale-invariant system identified by the screen, showing an increase in Lefty and dampening of Nodal signalling after extirpation. Simulations were fitted to the experimentally measured total length and mesendoderm extent (vertical red solid (untreated) and dashed (extirpated) lines). **d**, A parameter screen showing the influence of Lefty levels (σ_L), Nodal inhibition strength (λ) and Lefty induction steepness (κ_L) on scaling; the maximum projection through the six-dimensional parameter space is shown with the following discrete values: for σ_L : 0, 10^{-4} , 10^{-3} , 10^{-2} , 11.12, 22.23, 33.34, 44.45, 55.56, 66.67, 77.78, 88.89 and 10^2 ; for λ : 10^{-5} , 1.12×10^{-2} , 2.23×10^{-2} , 3.34×10^{-2} , 4.45×10^{-2} , 5.56×10^{-2} , 6.67×10^{-2} , 7.78×10^{-2} , 8.89×10^{-2} and 10^{-1} ; for κ_L : 10^2 , 1.12×10^5 , 2.23×10^5 , 3.34×10^5 , 4.45×10^5 , 5.56×10^5 , 6.67×10^5 , 7.78×10^5 , 8.89×10^5 and 10^6 . Parameter configurations that resulted in biologically unrealistic gradients were excluded. **e**, A parameter screen showing the influence of Lefty diffusivity on scaling; the maximum projection through the six-dimensional parameter space is shown. The model predicts that scaling should fail if Lefty induction (σ_L) or diffusion (D_L) is too low (that is, less than $\sim 7 \mu\text{m}^2 \text{s}^{-1}$).

adjustments in mesendoderm expansion dynamics over time rather than from shrinking an initially too broadly specified mesendodermal domain.

Scaling depends on Lefty levels. Our model predicted that scaling crucially depends on the levels of Lefty (Figs. 4d and 5a, b). To test

this prediction, we assessed mesendoderm proportions in embryos with varying numbers of functional *lft* alleles (*lft1* and *lft2*)³⁶. As expected, both untreated and extirpated double-homozygous *lft1*^{-/-}; *lft2*^{-/-} mutants showed dramatically increased Nodal signalling and an expanded mesendoderm³⁶ (Fig. 5c–g and Supplementary Fig. 3a–c). By contrast, untreated and shortened double-heterozygous

lft1^{+/-};lft2^{+/-} embryos exhibited nearly normal Nodal signalling and mesendoderm and ectoderm proportions, indicating that one functional allele of each *lft* is sufficient for proper spatial Nodal signalling and scaling, possibly due to dosage adjustments that result in similar amounts of protein (Fig. 5c–h and Supplementary Fig. 3a–c). Normally sized and extirpated single-homozygous *lft2^{-/-}* mutants had excess Nodal signalling and mesendoderm at the expense of the ectoderm (Fig. 5c–h and Supplementary Fig. 3a–c). By striking contrast, single-homozygous *lft1^{-/-}* embryos displayed expanded Nodal signalling and mesendoderm and a reduced ectoderm only after extirpation (Fig. 5c–h and Supplementary Fig. 3a–c). Interestingly, Lefty1 is less inhibitory than its paralogue Lefty2 (Supplementary Fig. 3d,e); thus, although highly active Lefty2 is sufficient for germ-layer patterning in normally sized embryos, the correct levels of less-active Lefty1 are required for scale-invariant patterning in substantially smaller embryos. These experimental findings support the simulations of our size-dependent inhibition model (Figs. 4d and 5a,b), showing that a small reduction in Lefty production, which does not significantly affect mesendoderm formation, abrogates scaling.

Scaling depends on highly diffusive Lefty. The second prediction of our model is that scaling depends on the high diffusivity of Lefty, which must reach the end of the patterning field (Figs. 4e and 6a,b). To test this prediction, we decreased Lefty diffusivity and determined the consequences on scaling. To obtain a patterning system in which the diffusion of Lefty1 can be experimentally manipulated, we first generated embryos in which the only source of Lefty was Lefty1-GFP (green fluorescent protein). We rescued *lft1^{-/-};lft2^{-/-}* double mutants by injecting highly precise and physiologically relevant amounts (see Methods for details) of *lft1-GFP* mRNA into the yolk syncytial layer (YSL) to mimic the secretion of endogenous Lefty from the marginal zone (Fig. 6c). Consistent with the high diffusivity of Lefty^{33,39}, Lefty1-GFP reached the end of the patterning field within 60 minutes after YSL injection (Fig. 6d,e and Supplementary Video 2). A large proportion of *lft1^{-/-};lft2^{-/-}* mutant embryos was rescued to adulthood with this method in normally sized (~70% fully or partially rescued) and extirpated (~60% fully or partially rescued) embryos (Fig. 6f–h and Supplementary Fig. 4a–d). Thus, Lefty1-GFP provided from the marginal zone is sufficient not only to pattern germ layers but also to allow scaling. Next, to hinder Lefty1-GFP diffusion, we used a ‘morphotrap’—an mCherry-labelled membrane-localized GFP-binding nanobody⁴⁰. Co-injection of mRNA encoding the morphotrap and *lft1-GFP* mRNA into one-cell-stage embryos changed the localization of Lefty1-GFP from uniform extracellular to strongly membrane associated (Supplementary Fig. 4e). Crucially, the diffusion coefficient (*D*) of Lefty1-GFP in embryos expressing the morphotrap was significantly lower ($D = 7.7 \pm 3.2 \mu\text{m}^2 \text{s}^{-1}$ for Lefty1-GFP and $0.2 \pm 0.2 \mu\text{m}^2 \text{s}^{-1}$ for Lefty1-GFP + morphotrap (mean \pm s.d.); Fig. 6i,j). In addition, the activity of Lefty was decreased by morphotrap binding (Supplementary Fig. 4f,g).

We then injected mRNA encoding the morphotrap into *lft1^{-/-};lft2^{-/-}* mutant embryos at the one-cell stage and generated local sources of Lefty1-GFP at the marginal zone (Fig. 6d,e). The expression of the morphotrap dramatically changed the range of Lefty1-GFP from a nearly uniform distribution to a short-range gradient that did not reach the end of the embryo (Fig. 6d,e and Supplementary Videos 2 and 3). In normally sized embryos, hindered Lefty diffusion did not significantly affect germ-layer patterning (Fig. 6f–h), possibly owing to decreased Lefty activity in the presence of morphotrap (Supplementary Fig. 4f,g). The change in Lefty distribution correlated with a steep drop in the rescue of extirpated embryos (Fig. 6f,g) and with an expanded mesendoderm (Fig. 6h and Supplementary Fig. 4c,d). Simulations of the size-dependent inhibition model with hindered Lefty diffusion recapitulated the

experimentally observed change in Lefty distribution (Fig. 6a,b,d,e): the decreased Lefty range precludes scaling of Nodal signalling as Lefty cannot reach the distal end of the patterning field. Together, these observations show that hindering Lefty diffusion prevents scaling in extirpated embryos, supporting the prediction of the size-dependent inhibition model.

Lefty concentration increases in smaller embryos. The third prediction of our model is that the inhibitor concentration increases to reduce Nodal signalling in extirpated embryos (Figs. 4c and 7a), whereas the total amount of Lefty should slightly decrease over time due to feedback regulation (Fig. 7b). To test this prediction, we used quantitative immunoblotting and measured the amount of endogenous Lefty1 and histone H3 as a proxy for cellular mass. Histone H3 levels were reduced by approximately one-third after extirpation (Supplementary Fig. 5a–c). Importantly, the histone H3 signal intensity increased proportionally when 5, 10 or 15 embryos were loaded, showing that changes in total protein can be detected reliably (Supplementary Fig. 5c). The decrease in Lefty1 amounts in extirpated embryos was less pronounced than histone H3 levels, resulting in an increased Lefty1 concentration as predicted by the model (Supplementary Fig. 5b). However, Lefty1 intensities detected by the only currently available antibody against a zebrafish Lefty³⁵ were low (Supplementary Fig. 5a and see Supplementary Fig. 8 for unprocessed data); sufficient Lefty1 levels could only be reliably detected after 50% epiboly stages, so that earlier dynamics of potential changes in Lefty1 levels could not be analysed. To corroborate these findings and to uncouple the rise in Lefty concentration from feedback regulation, we quantified the GFP intensity after injection of physiologically relevant amounts of *lft1-GFP* mRNA in the YSL and found that extirpated embryos exhibited a higher GFP intensity than normally sized embryos (Fig. 7c).

Exogenous inhibitor can mediate scaling in lieu of Lefty. To assess whether this increase in inhibitor concentration is required for germ-layer scaling, we analysed mesendoderm patterning in untreated and extirpated *lft1^{-/-};lft2^{-/-}* mutants upon exposure to the small-molecule Nodal inhibitor SB-505124 (ref. ³⁶). In contrast to the YSL injection rescue approach, a reduction in embryo size should not affect the concentration of the tonic Nodal inhibitor in this experimental setup (Supplementary Fig. 6a–d). A large fraction of untreated *lft1^{-/-};lft2^{-/-}* mutants (~90%; Fig. 7d,e) was rescued by 4.8 μM of Nodal inhibitor exposure. By contrast, exposure of extirpated *lft1^{-/-};lft2^{-/-}* mutants to the same inhibitor concentration resulted in abnormal mesendoderm proportions and only ~30% displayed some phenotypic rescue (Fig. 7d,e and Supplementary Fig. 6e,f). These results show that tonic size-independent inhibition levels that are effective in normally sized embryos do not allow scaling, as the inhibitor concentration cannot increase in shortened embryos.

Our model implies that increasing tonic Nodal inhibitor levels should restore the appropriate Nodal signalling range in extirpated embryos. Consistent with this prediction, increasing the exposure of the small-molecule Nodal inhibitor from 4.8 μM to 6–7 μM significantly improved the rescue of extirpated *lft1^{-/-};lft2^{-/-}* mutants from ~26% to ~64% (Fig. 7e and Supplementary Fig. 6g), demonstrating that increased inhibitor levels are required for scaling in extirpated embryos.

Discussion

Together, four lines of evidence suggest that scale-invariant germ-layer patterning is achieved by size-dependent inhibition of Nodal signalling. First, the reduction of Lefty levels (Fig. 5) precludes scaling. Second, decreasing Lefty diffusivity interferes with scale-invariant patterning (Fig. 6). Third, the concentration of the Nodal inhibitor Lefty increases in extirpated embryos (Fig. 7c and

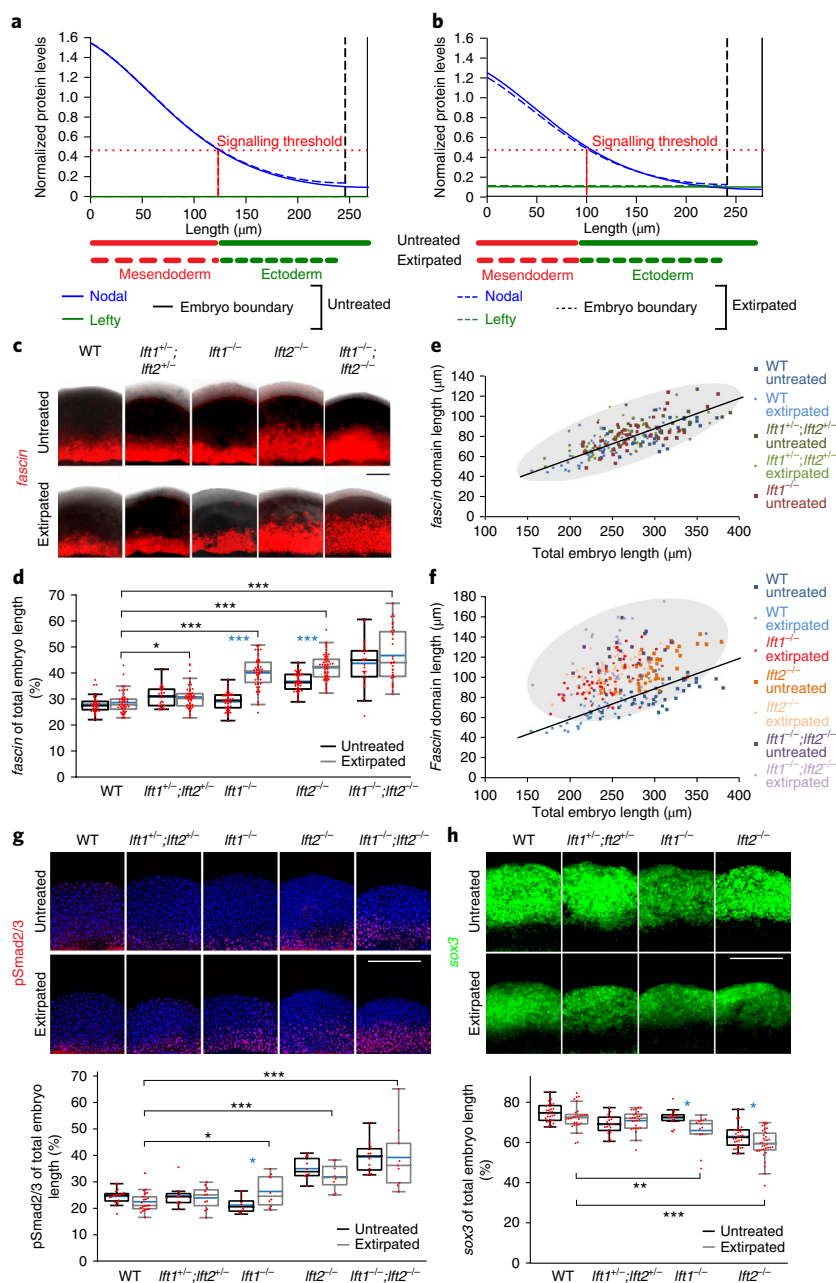


Fig. 5 | Germ-layer scaling depends on Lefty levels. **a,b**, Simulations of the size-dependent inhibition predict that, in the absence of Lefty, the mesoderm is extended and does not scale (**a**), whereas reduced Lefty induction should prevent scaling in shortened embryos without a significant change in mesoderm specification in normally sized individuals (**b**). **c**, Maximum intensity projections of lateral confocal stacks of *fascin* FISH in untreated and extirpated embryos with different numbers of *lft* alleles. **d**, Quantification of *fascin*-positive mesoderm proportions. The asterisks show differences between untreated and extirpated embryos (blue asterisks) and between WT and *lft* mutant extirpated embryos (black asterisks) (* $P < 0.05$, *** $P < 0.001$). **e,f**, Quantification of *fascin* relative to embryo length. The data for WT untreated and extirpated are plotted in both **e** and **f**. For the *lft* mutants, the encircled domains cluster two groups: group 1 shows a similar mesoderm proportion as WT individuals and a linear increase of mesoderm with embryo size (**e**), whereas group 2 clusters in a wider domain with larger mesodermal proportions, indicating an absence of scaling (**f**). In **c–f**, WT: n of untreated = 38, n of extirpated = 49; *lft1^{+/-};lft2^{+/-}*: n of untreated = 26, n of extirpated = 55; *lft1^{-/-}*: n of untreated = 50, n of extirpated = 58; *lft2^{-/-}*: n of untreated = 50, n of extirpated = 63; *lft1^{-/-};lft2^{-/-}*: n of untreated = 29, n of extirpated = 34. **g,h**, Maximum intensity projections of lateral confocal pSmad2/3 immunostaining (**g**) and *sox3* FISH stacks (**h**), and quantification in 2 hpe embryos with different numbers of *lft* alleles. For pSmad2/3: WT: n of untreated = 19, n of extirpated = 21; *lft1^{+/-};lft2^{+/-}*: n of untreated = 10, n of extirpated = 11; *lft1^{-/-}*: n of untreated = 8, n of extirpated = 10; *lft2^{-/-}*: n of untreated = 9, n of extirpated = 8; *lft1^{-/-};lft2^{-/-}*: n of untreated = 12, n of extirpated = 9. For *sox3*: WT: n of untreated = 28, n of extirpated = 28; *lft1^{+/-};lft2^{+/-}*: n of untreated = 21, n of extirpated = 27; *lft1^{-/-}*: n of untreated = 14, n of extirpated = 13; *lft2^{-/-}*: n of untreated = 30, n of extirpated = 33. The asterisks show differences between untreated and extirpated embryos (blue asterisks) and between extirpated WT and *lft* mutant embryos (black asterisks) (* $P < 0.05$; ** $P < 0.01$; *** $P < 0.001$). The box plots show the median (blue line), the mean (black (untreated) and grey (extirpated) lines), 25% and 75% quantiles (box) and all included data points (red markers). Whiskers extend to the smallest data point within the 1.5 interquartile range of the lower quartile and to the largest data point within the 1.5 interquartile range of the upper quartile. Two-sided Student's t -tests were performed ($\alpha = 0.05$). See Supplementary Table 1 for statistics source data. Scale bars, 70 μm (**c**) and 200 μm (**g,h**).

Supplementary Fig. 5b). Fourth, the rescue of extirpated *lft1*^{-/-};*lft2*^{-/-} mutants requires higher amounts of a Nodal inhibitor drug than non-extirpated mutants (Fig. 7e and Supplementary Fig. 6g). In agreement with our mathematical model (Fig. 4, Supplementary Fig. 7 and Supplementary Note 1), these results support the idea that the concentration and high diffusivity of Lefty are essential to adjust germ-layer proportions.

The initial computational screen used *fascin* as a proxy for mesendoderm formation, which, in addition to Nodal, is also under the control of fibroblast growth factor (FGF) signalling^{10,35}. For the simplified screening model, we subsumed the action of Nodal and FGF into one effective signalling gradient, as the induction of both *fgf* and *fascin* depends on Nodal signalling^{35,41–44}, Nodal and FGF signals have similar effective mobilities in zebrafish embryos^{33,39}, and the range of *fascin* can be changed by Lefty-dependent modulation of Nodal signalling^{32,33}. Thus, our conclusions are not affected by how FGF, acting downstream of Nodal signalling, helps to regulate

fascin expression together with Nodal. In more-refined simulations, we demonstrate the plausibility of our model for Nodal signalling based on pSmad2/3 activity (Supplementary Fig. 7m,n), a direct readout of Nodal activity. Although tissue proportions might be further refined by interactions with other signalling pathways, such as bone morphogenetic protein (BMP) and FGF^{10,35,43,45} (Supplementary Fig. 7o,p and Supplementary Note 1), the scaled distribution of the Nodal signal transducer pSmad2—which is independent of BMP and FGF—and the scaled tissue proportions in *lft* mutants rescued by feedback-uncoupled Lefty—in which Lefty production is not under any transcriptional regulation—demonstrate the central role of Lefty in germ-layer scaling.

In agreement with previous findings^{10,36,46,47}, our results suggest that Nodal-mediated germ-layer patterning is robust to variations in signalling. Although the mesendoderm is significantly expanded in *lft1*^{-/-} extirpated and *lft2*^{-/-} untreated embryos (Supplementary Fig. 3c), most of them develop with normal morphology (Fig. 5 and

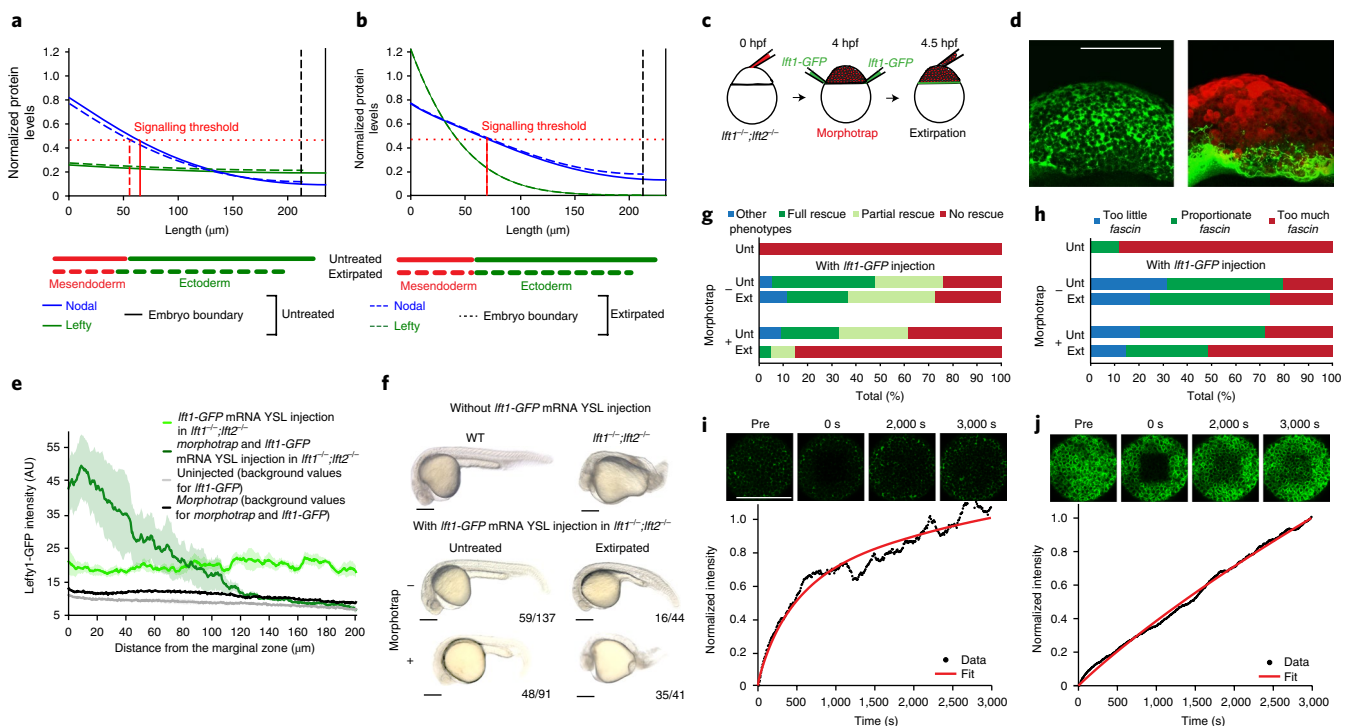


Fig. 6 | High Lefty diffusivity is required for scaling. **a, b**, Simulations of the model without feedback inhibition (*lft1-GFP* injected in the YSL; **a**) and hindered Lefty diffusion (morphotrap binds to *lft1-GFP*; **b**) predict that a reduction in Lefty diffusivity—preventing Lefty from reaching the animal pole—should preclude scaling. **c**, Schematic of morphotrap-mediated Lefty1-GFP diffusion hindrance in extirpated embryos. **d**, Maximum intensity projections of confocal stacks of *lft1*^{-/-};*lft2*^{-/-} embryos injected with (right panel) morphotrap (injected at the one-cell stage) and *lft1-GFP* mRNA in the YSL (injected at the sphere stage). Lateral views are shown. **e**, Spatial distribution of Lefty1-GFP secreted from the YSL. The morphotrap prevents spreading of Lefty1-GFP towards the animal pole of the embryo. *n* of *lft1-GFP* mRNA injection = 6, *n* of *morphotrap* + *lft1-GFP* mRNA injection = 3, *n* of background values = 1, *n* of background values for morphotrap = 2. The experimentally determined distributions of Lefty1-GFP with morphotrap-mediated diffusion hindrance resemble the simulation of the scenario in **b**. The shaded regions are the s.e.m. **f**, Lateral views of representative 26 hpf *lft1*^{-/-};*lft2*^{-/-} embryos with different treatments. The numbers in the figure panel indicate the fraction of these representative embryos. **g**, Phenotype distributions in *lft1*^{-/-};*lft2*^{-/-} embryos after different treatments (*n* of *lft1*^{-/-};*lft2*^{-/-} = 39; *lft1*^{-/-};*lft2*^{-/-} + *lft1-GFP*: *n* of untreated (Unt) = 137, *n* of extirpated (Ext) = 44; *lft1*^{-/-};*lft2*^{-/-} + *morphotrap* + *lft1-GFP*: *n* of untreated = 91, *n* of extirpated = 44). Embryos with partial rescue display imperfect tails and reduced cephalic structures (that is, very mild Lefty mutant phenotypes). **h**, The fraction of treated *lft1*^{-/-};*lft2*^{-/-} embryos with low (<22%), normal (22–33%) and high (>34%) mesendoderm proportions (*n* of *lft1*^{-/-};*lft2*^{-/-} = 44; *lft1*^{-/-};*lft2*^{-/-} + *lft1-GFP*: *n* of untreated = 67, *n* of extirpated = 66; *lft1*^{-/-};*lft2*^{-/-} + *morphotrap* + *lft1-GFP*: *n* of untreated = 35, *n* of extirpated = 37). The fraction of rescued and non-rescued *lft1*^{-/-};*lft2*^{-/-} embryos correlates with the fraction of normal and high mesendoderm proportions in **g** and **h**. **i, j**, FRAP experiments demonstrate that Lefty1-GFP diffusion is hindered by the morphotrap. Representative FRAP data for Lefty1-GFP (**i**) and Lefty1-GFP with morphotrap (**j**) are shown. Microscopy images are shown before photobleaching (Pre), immediately after (0 s), as well as at 2,000 s and 3,000 s after photobleaching. Diffusion coefficients and production rates were fitted to the recovery curves using previously published values for Lefty1-GFP protein stability³³. The mean (±s.d.) diffusion coefficients were $7.7 \pm 3.2 \mu\text{m}^2 \text{s}^{-1}$ for Lefty1-GFP (from *n* = 6 independent experiments) and $0.2 \pm 0.2 \mu\text{m}^2 \text{s}^{-1}$ for Lefty1-GFP with morphotrap (from *n* = 4 independent experiments). See Supplementary Table 1 for statistics source data. Scale bars, 200 μm (**d, f, i, j**).

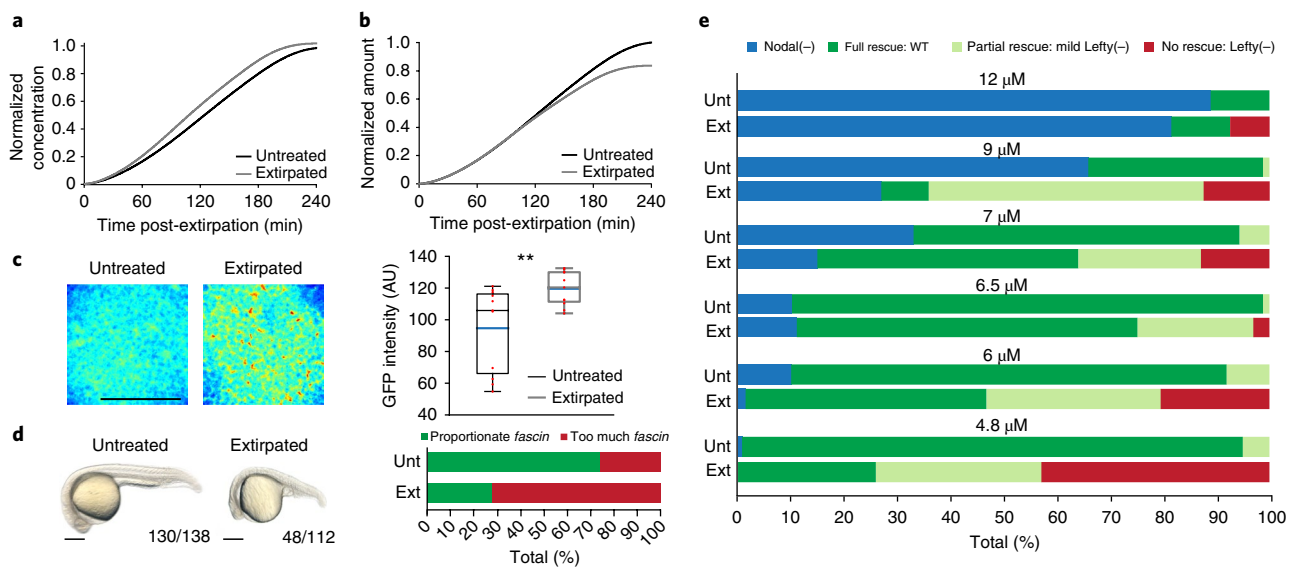


Fig. 7 | Lefty concentration increases in smaller embryos to allow scaling. **a**, The increase in Lefty concentration over time in smaller embryos predicted by the size-dependent inhibition model. **b**, The decrease in Lefty amount over time in smaller embryos predicted by the size-dependent inhibition model. **c**, Animal pole views of the maximum intensity confocal stack projections of WT untreated and extirpated embryos injected with *lft1*-GFP mRNA in the YSL (left) and the quantification of GFP intensity; ** $P < 0.01$; n of untreated = 11, n of extirpated = 11 (right). The box plot shows the median (blue line), the mean (black (untreated) and grey (extirpated) lines), 25% and 75% quantiles (box) and all included data points (red markers). Whiskers extend to the smallest data point within the 1.5 interquartile range of lower quartile and to the largest data point within the 1.5 interquartile range of the upper quartile. Two-sided Student's *t*-test were performed ($\alpha = 0.05$). **d**, Lateral views of representative 26 hpf *lft1*^{-/-}/*lft2*^{-/-} embryos exposed to 4–4.8 μ M of the Nodal inhibitor SB-505124. The numbers in the figure panel indicate the fraction of these representative embryos. Mesendoderm quantification (right panel) of *lft1*^{-/-}/*lft2*^{-/-} embryos exposed to 4–4.8 μ M of the Nodal inhibitor SB-505124 (n of untreated (Unt) = 27, n of extirpated (Ext) = 18). **e**, Phenotype quantification in *lft1*^{-/-}/*lft2*^{-/-} embryos exposed to different concentrations of the Nodal inhibitor SB-505124. Untreated: 4.8 μ M: $n = 138$, 6 μ M: $n = 160$, 6.5 μ M: $n = 80$, 7 μ M: $n = 106$, 9 μ M: $n = 85$, 12 μ M: $n = 36$. Extirpated: 4.8 μ M: $n = 77$, 6 μ M: $n = 146$, 6.5 μ M: $n = 64$, 7 μ M: $n = 108$, 9 μ M: $n = 56$, 12 μ M: $n = 27$. Exposure to higher concentrations of the Nodal inhibitor SB-505124 increases *lft1*^{-/-}/*lft2*^{-/-} mutant rescue after extirpation. The fraction of rescued and non-rescued *lft1*^{-/-}/*lft2*^{-/-} embryos correlates with the fraction of normal and high mesendoderm proportions in **d**. See Supplementary Table 1 for statistics source data. Scale bars, 200 μ m (**c,d**).

Supplementary Fig. 3b). This suggests that embryos can adapt to a certain degree of mesendoderm expansion, possibly up to ~42% (Supplementary Fig. 3a–c). However, this margin of tolerance is reduced in *lft1*^{-/-}/*lft2*^{-/-} embryos rescued with YSL-expressed Lefty1-GFP, and an increase in the mesendoderm domain above ~35% in this context seems to invariably prevent phenotypic rescue. Thus, patterning robustness might arise from Nodal–Lefty regulatory feedback, which is absent in *lft1*^{-/-}/*lft2*^{-/-} mutant embryos but present in embryos with at least one intact Lefty paralogue.

Previously postulated feedback-dependent scaling systems rely on modulators whose concentrations change depending on tissue size to adjust the signalling activity range by modulating the diffusivity or clearance of the signal^{11,14,48–56}. The Nodal–Lefty activator–inhibitor system is an excellent candidate for a modulator-based scaling mechanism: (1) Lefty (modulator) inhibits Nodal activity by binding and preventing it from activating its receptors, (2) the Nodal activity range is unaffected by the size reduction in extirpated embryos, as the Nodal distribution is restricted to the marginal zone owing to its low diffusivity³³, (3) Lefty diffuses significantly faster than Nodal and exhibits a nearly uniform distribution^{33,36} (Figs. 4c and 6d,e,i and Supplementary Video 2), and (4) the production of Lefty is largely independent of the changes in size as Lefty-producing cells are located at the margin, which remains unaffected immediately following extirpation (Fig. 3e–i). An example of a modulator-based scaling mechanism is the recently proposed ‘expansion–repression’ model, in which scaling of signalling gradients is achieved by an expander that increases the range of the signal and that is itself repressed by the signal⁵¹. Superficially, our model can be interpreted as a mirror image of the

‘expansion–repression’ model—that is, a ‘contraction–activation’ system—as the ‘inhibitor’ (or the ‘contractor’) Lefty restricts the range of the signal (Nodal) and is activated by the signal. However, our theoretical model does not depend on feedback between the signal and the modulator. Because in our system the modulator inhibits the signal, it is sufficient to couple the changes in the concentration of the inhibitor to size to confer proportionate patterning. Similarly, we showed experimentally that Nodal-mediated Lefty activation is dispensable for scaling (Figs. 6 and 7 and Supplementary Figs. 4 and 6). This suggests that scale-invariant patterning is purely based on size-dependent Nodal inhibition that is mediated by Lefty, providing a foundation for the proportionate allocation of all future tissues.

The scaling mechanism that we found crucially depends on the coupling of the inhibitor concentration to embryo size, which is conferred by the high diffusivity of Lefty. Strikingly, a similar mechanism based on the coupling of cell volume to the concentration of a cell-cycle inhibitor has recently been found to control cell size in yeast⁵⁷. Thus, it is possible that this simple mechanism might be widespread across various levels of biological organization to coordinate growth with cellular functions and patterning.

Methods

Methods, including statements of data availability and any associated accession codes and references, are available at <https://doi.org/10.1038/s41556-018-0155-7>.

Received: 2 August 2017; Accepted: 27 June 2018;

Published online: 30 July 2018

References

- Morgan, T. H. Half embryos and whole embryos from one of the first two blastomeres. *Anat. Anz.* **10**, 623–685 (1895).
- Cooke, J. Control of somite number during morphogenesis of a vertebrate, *Xenopus laevis*. *Nature* **254**, 196–199 (1975).
- Inomata, H. Scaling of pattern formations and morphogen gradients. *Dev. Growth Differ.* **59**, 41–51 (2017).
- García, M., Nahmad, M., Reeves, G. T. & Stathopoulos, A. Size-dependent regulation of dorsal–ventral patterning in the early *Drosophila* embryo. *Dev. Biol.* **381**, 286–299 (2013).
- Lauschke, V. M., Tsiarlis, C. D., Francois, P. & Aulehla, A. Scaling of embryonic patterning based on phase-gradient encoding. *Nature* **493**, 101–105 (2013).
- Kicheva, A. et al. Kinetics of morphogen gradient formation. *Science* **315**, 521–525 (2007).
- Wartlick, O., Kicheva, A. & González-Gaitán, M. Morphogen gradient formation. *Cold Spring Harb. Perspect. Biol.* **1**, a001255 (2009).
- Yu, S. R. et al. Fgf8 morphogen gradient forms by a source–sink mechanism with freely diffusing molecules. *Nature* **461**, 533–536 (2009).
- Rogers, K. W. & Schier, A. F. Morphogen gradients: from generation to interpretation. *Annu. Rev. Cell Dev. Biol.* **27**, 377–407 (2011).
- Rogers, K. W. & Müller, P. Nodal and BMP dispersal during early zebrafish development. *Dev. Biol.* <https://doi.org/10.1016/j.ydbio.2018.04.002> (2018).
- Umulis, D. M. & Othmer, H. G. Mechanisms of scaling in pattern formation. *Development* **140**, 4830–4843 (2013).
- Gregor, T., Bialek, W., de Ruyter van Steveninck, R. R., Tank, D. W. & Wieschaus, E. F. Diffusion and scaling during early embryonic pattern formation. *Proc. Natl Acad. Sci. USA* **102**, 18403–18407 (2005).
- Gregor, T., McGregor, A. P. & Wieschaus, E. F. Shape and function of the bicoid morphogen gradient in dipteran species with different sized embryos. *Dev. Biol.* **316**, 350–358 (2008).
- Ben-Zvi, D., Shilo, B.-Z., Fainsod, A. & Barkai, N. Scaling of the BMP activation gradient in *Xenopus* embryos. *Nature* **453**, 1205–1211 (2008).
- Ben-Zvi, D., Pyrowolakis, G., Barkai, N. & Shilo, B. Z. Expansion–repression mechanism for scaling the Dpp activation gradient in *Drosophila* wing imaginal discs. *Curr. Biol.* **21**, 1391–1396 (2011).
- Hamaratoglu, F., de Lachapelle, A. M., Pyrowolakis, G., Bergmann, S. & Affolter, M. Dpp signaling activity requires pentagone to scale with tissue size in the growing *Drosophila* wing imaginal disc. *PLoS Biol.* **9**, e1001182 (2011).
- Wartlick, O. et al. Dynamics of Dpp signaling and proliferation control. *Science* **331**, 1154–1159 (2011).
- Cheung, D., Miles, C., Kreitman, M. & Ma, J. Scaling of the bicoid morphogen gradient by a volume-dependent production rate. *Development* **138**, 2741–2749 (2011).
- Wartlick, O., Jülicher, F. & González-Gaitán, M. Growth control by a moving morphogen gradient during *Drosophila* eye development. *Development* **141**, 1884–1893 (2014).
- Kicheva, A. et al. Coordination of progenitor specification and growth in mouse and chick spinal cord. *Science* **345**, 1254927 (2014).
- Uygun, A. et al. Scaling pattern to variations in size during development of the vertebrate neural tube. *Dev. Cell* **37**, 127–135 (2016).
- Schulte-Merker, S. et al. Expression of zebrafish gooseoid and no tail gene products in wild-type and mutant no tail embryos. *Development* **120**, 843–852 (1994).
- Schier, A. F. Nodal morphogens. *Cold Spring Harb. Perspect. Biol.* **1**, a003459 (2009).
- Chen, C. & Shen, M. M. Two modes by which Lefty proteins inhibit Nodal signaling. *Curr. Biol.* **14**, 618–624 (2004).
- Feldman, B. et al. Zebrafish organizer development and germ-layer formation require Nodal-related signals. *Nature* **395**, 181–185 (1998).
- Rebagliati, M. R., Toyama, R., Fricke, C., Haffter, P. & Dawid, I. B. Zebrafish Nodal-related genes are implicated in axial patterning and establishing left–right asymmetry. *Dev. Biol.* **199**, 261–272 (1998).
- Sampath, K. et al. Induction of the zebrafish ventral brain and floorplate requires Cyclops/Nodal signalling. *Nature* **395**, 185–189 (1998).
- Meno, C. et al. Mouse Lefty2 and zebrafish antivin are feedback inhibitors of nodal signaling during vertebrate gastrulation. *Mol. Cell* **4**, 287–298 (1999).
- Feldman, B. et al. Lefty antagonism of Squint is essential for normal gastrulation. *Curr. Biol.* **12**, 2129–2135 (2002).
- Chen, Y. & Schier, A. F. Lefty proteins are long-range inhibitors of Squint-mediated Nodal signaling. *Curr. Biol.* **12**, 2124–2128 (2002).
- Cheng, S. K., Olale, F., Brivanlou, A. H. & Schier, A. F. Lefty blocks a subset of TGF β signals by antagonizing EGF-CFC coreceptors. *PLoS Biol.* **2**, e30 (2004).
- Choi, W. Y., Giraldez, A. J. & Schier, A. F. Target protectors reveal dampening and balancing of Nodal agonist and antagonist by miR-430. *Science* **318**, 271–274 (2007).
- Müller, P. et al. Differential diffusivity of Nodal and Lefty underlies a reaction–diffusion patterning system. *Science* **336**, 721–724 (2012).
- Wang, Y., Wang, X., Wohland, T. & Sampath, K. Extracellular interactions and ligand degradation shape the Nodal morphogen gradient. *eLife* **5**, e13879 (2016).
- van Boxtel, A. L. et al. A temporal window for signal activation dictates the dimensions of a Nodal signaling domain. *Dev. Cell* **35**, 175–185 (2015).
- Rogers, K. W. et al. Nodal patterning without Lefty inhibitory feedback is functional but fragile. *eLife* **6**, e28785 (2017).
- Xu, C. et al. Nanog-like regulates endoderm formation through the Mxtx2–Nodal pathway. *Dev. Cell* **22**, 625–638 (2012).
- Marcon, L., Diego, X., Sharpe, J. & Müller, P. High-throughput mathematical analysis identifies Turing networks for patterning with equally diffusing signals. *eLife* **5**, e14022 (2016).
- Müller, P., Rogers, K. W., Yu, S. R., Brand, M. & Schier, A. F. Morphogen transport. *Development* **140**, 1621–1638 (2013).
- Harmansa, S., Hamaratoglu, F., Affolter, M. & Caussinus, E. Dpp spreading is required for medial but not for lateral wing disc growth. *Nature* **527**, 317–322 (2015).
- Gritsman, K. et al. The EGF-CFC protein one-eyed pinhead is essential for Nodal signaling. *Cell* **97**, 121–132 (1999).
- Mathieu, J. et al. Nodal and Fgf pathways interact through a positive regulatory loop and synergize to maintain mesodermal cell populations. *Development* **131**, 629–641 (2004).
- Bennett, J. T. et al. Nodal signaling activates differentiation genes during zebrafish gastrulation. *Dev. Biol.* **304**, 525–540 (2007).
- Liu, Z. et al. Fscn1 is required for the trafficking of TGF- β family type I receptors during endoderm formation. *Nat. Commun.* **7**, 12603 (2016).
- van Boxtel, A. L., Economou, A. D., Heliot, C. & Hill, C. S. Long-range signaling activation and local inhibition separate the mesoderm and endoderm lineages. *Dev. Cell* **44**, 179–191 (2018).
- Dougan, S. T. The role of the zebrafish Nodal-related genes squint and cyclops in patterning of mesendoderm. *Development* **130**, 1837–1851 (2003).
- Pei, W., Williams, P. H., Clark, M. D., Stemple, D. L. & Feldman, B. Environmental and genetic modifiers of septum penetrance during zebrafish embryogenesis. *Dev. Biol.* **308**, 368–378 (2007).
- Gierer, A. & Meinhardt, H. A theory of biological pattern formation. *Kybernetik* **12**, 30–39 (1972).
- Othmer, H. G. & Pate, E. Scale-invariance in reaction–diffusion models of spatial pattern formation. *Proc. Natl Acad. Sci. USA* **77**, 4180–4184 (1980).
- Francois, P., Vonica, A., Brivanlou, A. H. & Siggia, E. D. Scaling of BMP gradients in *Xenopus* embryos. *Nature* **461**, E1 (2009).
- Ben-Zvi, D. & Barkai, N. Scaling of morphogen gradients by an expansion–repression integral feedback control. *Proc. Natl Acad. Sci. USA* **107**, 6924–6929 (2010).
- Umulis, D. M. Analysis of dynamic morphogen scale invariance. *J. R. Soc. Interface* **6**, 1179–1191 (2009).
- Inomata, H., Shibata, T., Haraguchi, T. & Sasai, Y. Scaling of dorsal–ventral patterning by embryo size-dependent degradation of Spemann’s organizer signals. *Cell* **153**, 1296–1311 (2013).
- Ben-Zvi, D., Fainsod, A., Shilo, B. Z. & Barkai, N. Scaling of dorsal–ventral patterning in the *Xenopus laevis* embryo. *Bioessays* **36**, 151–156 (2014).
- Werner, S. et al. Scaling and regeneration of self-organized patterns. *Phys. Rev. Lett.* **114**, 138101 (2015).
- Rasolonjanahary, M. & Vasiev, B. Scaling of morphogenetic patterns in reaction–diffusion systems. *J. Theor. Biol.* **404**, 109–119 (2016).
- Schmoller, K. M., Turner, J. J., Koivomagi, M. & Skotheim, J. M. Dilution of the cell cycle inhibitor Whi5 controls budding-yeast cell size. *Nature* **526**, 268–272 (2015).

Acknowledgements

We thank C. Hill for providing the Lefty1 antibody, M. Affolter for providing the morphotrap construct and J. Raspopovic and N. Lord for helpful comments. This work was supported by EMBO (M.A.-C., L.M. and P.M.) and HFSP (P.M.) long-term fellowships, the NSF Graduate Research Fellowship Program (K.W.R.), NIH grant GM56211 (A.F.S.), and funding from the Max Planck Society, ERC Starting Grant 637840 and HFSP Career Development Award CDA00031/2013-C (P.M.).

Author contributions

M.A.-C., A.F.S. and P.M. conceived the study. P.M. developed the extirpation assay and supervised the project. G.H.S. developed the extirpation device and the 2D map visualization workflow and optimized the pSmad2/3 immunostaining protocol. D.M. performed the experiments in Fig. 6i,j, Supplementary Figs. 4f,g, 5 and 8 and contributed to experiments in Fig. 6f,h. K.W.R. and A.F.S. contributed the data in Supplementary

Fig. 3d,e and provided the *lft* mutants before publication. M.A.-C. performed all other experiments. M.A.-C., A.B., D.M. and P.M. analysed the data. A.F.S. and P.M. conceptualized the scaling model. A.B. performed the mathematical analysis and simulations with assistance from L.M. and P.M. M.A.-C. and P.M. wrote the manuscript with input from all authors.

Competing interests

The authors declare no competing interests.

Additional information

Supplementary information is available for this paper at <https://doi.org/10.1038/s41556-018-0155-7>.

Reprints and permissions information is available at www.nature.com/reprints.

Correspondence and requests for materials should be addressed to P.M.

Publisher's note: Springer Nature remains neutral with regard to jurisdictional claims in published maps and institutional affiliations.

Methods

Generating smaller embryos by extirpation. All procedures involving animals were executed in accordance with the guidelines of the State of Baden-Württemberg (Germany) and approved by the Regierungspräsidium Tübingen (35/9185.46-5 and 35/9185.81-5).

Extirpation assays were performed using a glass capillary holder mounted on a Hamilton syringe and fixed in a micromanipulator (Narishige). Extirpations were performed in 4-hpf pronase-dechorionated sphere-stage embryos in Ringer's solution (116 mM NaCl, 2.8 mM KCl, 1 mM CaCl₂ and 5 mM HEPES). To allow wound healing after extirpation, embryos were left undisturbed for 30 min at 28 °C. The wound typically healed within 15 min after extirpation and the extirpated embryos were then transferred to normal embryo medium. To assess the survival of extirpated embryos without considering other mechanical disruptions of the extirpation assay (such as wound-healing failure or mechanical constraints due to changes in the embryo/yolk ratio), embryos that did not survive extirpation or that did not proceed to gastrulation were discarded.

For the quantification of cell numbers, extirpated cells from pools of ten embryos were transferred to individual PCR tubes containing 0.05% trypsin solution (Gibco) and incubated for 15 min at 37 °C. Dissociated cells were then quantified using a Neubauer chamber on an Olympus CKX41 microscope. Pools (10–20) of extirpated cells from 10 embryos were quantified per extirpation experiment. The average number of extirpated cells per embryo was 820 ± 130 cells, which corresponds to ~30% of the cells of an embryo at the sphere stage with ~3,000 cells.

Whole-mount in situ hybridization. *fascin*, *hgg1*, *vsx2*, *sox3*, *sox17* and *sox32* RNA probes for in situ hybridization assays were synthesized using SP6 or T7 polymerase (Roche) and digoxigenin (DIG)-modified (Roche) or dinitrophenol (DNP)-modified (Perkin Elmer) ribonucleotides. RNA probes were purified by ethanol precipitation with 7.5 M lithium chloride. For chromogenic in situ hybridizations, embryos were fixed overnight at 4 °C in 4% formaldehyde and then processed using an In situ Pro hybridization robot (Abimed/Intavis) and, as previously described³⁶, with the following modifications: no proteinase K treatment before the 90% epiboly stage; no pre-absorption of the anti-DIG antibody (11093274910, Roche); 5% dextran sulfate (Sigma) added to the hybridization solution³⁹; riboprobes were denatured at 80 °C for 15 min and chilled on ice prior to hybridization using a final concentration of 1–2 ng μ l⁻¹.

For fluorescent in situ hybridization (FISH), the following modifications were used: the blocking solution contained 2% Blocking Reagent (Roche) in 1× MABT_w; incubation with anti-DIG (Roche) or anti-DNP-POD (FP1129, Perkin-Elmer) antibodies at a dilution of 1:150 in blocking solution was carried out overnight with shaking at 4 °C; after antibody incubation, embryos were washed six times for 20–30 min at room temperature with PBS containing 0.1% Tween (PBST) and the signal was developed with 100 μ l TSA Cy3 or Cy5 at a dilution of 1:75 in amplification buffer (Perkin Elmer) for 1 h at room temperature without shaking.

For imaging, embryos were embedded in 1% low-melting point agarose, transferred to glass-bottom culture dishes (MatTek corporation) and oriented manually. Only embryos that were mounted with the vegetal–animal axis completely parallel to the cover glass were used for analysis. For chromogenic in situ samples, images were captured using an Axio Zoom.V16 (Zeiss). For fluorescent in situ samples, confocal laser scanning microscopy was performed using an LSM 780 NLO microscope (Zeiss). Images were processed using Fiji⁶⁰. The number of *hgg1*-, *sox17*- and *sox32*-positive cells was quantified using the 'multi-point selection' tool⁶⁰. *fascin* and *sox3* expression domains^{44,61} in the central-most embryo regions were quantified using the 'measure' tool in Fiji. *fascin* was quantified from the margin of the embryo to the end of the domain with high expression values. *sox3* was quantified from the animal pole to the end of the domain with high expression values. The shield was excluded in the selection due to a higher expression of mesendodermal markers in this region. The size of embryos (from the margin to the animal pole) was measured similarly using bright-field images.

Immunostaining. For immunostainings, anti-phospho-histone H3 (anti-pH3; 3377S, Cell Signaling Technologies) and anti-pSmad2/3 (8828, Cell Signaling Technologies) antibodies were used.

Immunostaining for pH3 was carried out as described previously⁶² with a 1:500 dilution of the primary antibody. For pSmad2/3, specimens were incubated in cold acetone at –20 °C for 20 min before blocking³⁵. To ensure staining specificity, samples were exposed to low concentrations of anti-pSmad2/3 antibody (1:2,000 or 1:5,000) and samples were washed for 24 h with PBST before adding the secondary antibody. The signal was then amplified using horseradish peroxidase (HRP)-conjugated anti-rabbit antibodies (111-035-003, Jackson ImmunoResearch) and TSA Cy3 or Cy5 at a dilution of 1:75 in amplification buffer (Perkin Elmer) for 45 min at room temperature without shaking. Embryos were mounted for imaging as described above for FISH, but with the dorsal–ventral axis parallel to the cover glass in the case of pH3 staining. Confocal laser scanning microscopy was performed using an LSM 780 NLO (Zeiss) confocal microscope and images were processed using Fiji. The number of pH3-positive cells was quantified over a depth of 140 μ m using the 'find maxima' plug-in in Fiji, with a fixed noise

tolerance of 10,000 and manual correction. pSmad2/3 distributions were quantified from the margin of the embryo to the end of the pSmad2/3 nuclear staining using the 'measure' tool in Fiji. Non-nuclear staining was excluded. The extent of pSmad2/3 signalling was variable along the embryonic margin, and the mean of the pSmad2/3 domain at ten different points along the marginal zone is shown in all figures. The size of embryos from the margin to the animal pole was measured similarly using 4,6-diamidino-2-phenylindole (DAPI)-stained images.

Cell density quantification. Cell density measurements were performed in untreated and extirpated H2A-GFP⁶³ transgenic embryos. Embryos were mounted at 1 hpe and 2 hpe as described above for pH3 immunostaining. The number of cells was quantified as described above for pH3-positive cells but over a depth of 80 μ m. The automatic segmentation and assignment of nuclei within the highly dense field of cells were carefully inspected visually and manually corrected.

Epiboly measurements. Untreated and extirpated embryos were imaged every 30 min after extirpation. Lateral images were taken. The extent of the embryo proper, the uncovered yolk, the blastoderm thickness and the total length (embryo proper + yolk) were measured. To calculate the percentage of epiboly, the percentage of the total length that was covered by the embryo proper was calculated. Blastoderm spreading during epiboly was calculated by subtracting the extent of the embryo proper at 1.5, 2, 3 and 4 hpe from the embryo proper extent at the first time point of analysis (1 hpe).

Light-sheet imaging for 3D reconstructions of *fascin* and pSmad2/3 domains.

For 3D imaging, a Light-sheet Z.1 microscope (Zeiss) was used. Embryos were embedded in 1% low-melting point agarose and mounted in glass capillaries. For merging of the different views, far-red or green fluorescent beads (Thermo Fischer Scientific) were added to the agarose at a 1:200,000 dilution. After 3D reconstruction, 2D maps were generated as described previously⁶⁴ and rotated to the correct perspective using Hugin panorama photo stitcher software (<http://hugin.sourceforge.net>).

To quantify the signal distribution in the resulting 2D maps, images were opened in Fiji and rotated by 90°. The region corresponding to the whole embryo was selected, and the average intensity of *fascin* or pSmad2/3 from every point of the embryonic vegetal–animal axis was obtained using the 'plot profile' plug-in in Fiji. Distances in pixels were transformed into percentages of the total embryo length with the vegetal-most side defined as 0% and the animal-most side as 100%. Intensity was then normalized by subtracting background values (that is, the lowest intensity value closest to the animal pole of the embryo) and setting the highest intensity value to 1. For the quantification of pSmad2/3 distributions, background values were obtained by imaging *lefty* mRNA-injected embryos after pSmad2/3 immunostaining and normalized using the highest intensity value from the uninjected experimental data sets. 2D maps of DAPI were used as controls to rule out spatial inhomogeneities along the embryonic vegetal–animal axis. The graphs in Figs. 1e and 3b represent scaled average maps obtained from several embryos.

To re-dimensionalize the scaled 2D maps (Figs. 1g and 3d), distances were multiplied by the measured embryo diameter and divided by $\pi/2$. Intensities were averaged in bins of 2 μ m, and the mean and standard error of different individuals were calculated piece wise.

Assessment of *Lefty1* and *Lefty2* activity. mRNA encoding *Lefty1*-GFP or *Lefty2*-GFP³³ was generated by plasmid linearization with NotI (NEB), purification with a Qiagen PCR clean-up kit and in vitro transcription using SP6 mMessage mMachine kits (Ambion). Pronase-dechorionated wild-type (WT; TLAB) embryos at the one-cell stage were injected with different amounts of *lft1*-GFP (22 pg, 43 pg and 86 pg) or *lft2*-GFP (5 pg, 10 pg and 20 pg) mRNA along with 100 pg of 10 kDa Alexa546-dextran (Life Technologies). At the sphere stage, three to five embryos per condition were imaged on an LSM 780 (Zeiss) confocal laser scanning microscope, and eight embryos with three replicates per condition were collected for qRT-PCR at 50% epiboly. Extracellular fluorescence intensity quantifications and qRT-PCR measurements with Promega Go-Taq qPCR Master Mix were executed as described previously³³ using the zebrafish elongation factor *ef1a* as a normalization control.

Immunoblotting. WT (TE strain) zebrafish embryos around the 50% epiboly stage were deyolked manually with tweezers and a dissection needle. 'Negative control' embryos were treated from 4-cell to 8-cell stages onward with the Nodal inhibitor SB-505124 (S4696, Sigma Aldrich) at 50 μ M as described previously³⁵. The efficiency of inhibitor treatment was confirmed by assessing the phenotypes of inhibitor-treated and dimethylsulfoxide-treated embryos at 24 hpf. 'Positive control' embryos were injected with 10 pg Squint-encoding mRNA³³ to induce endogenous *lft1* expression and were staged according to the development of uninjected siblings. Deyolked embryo caps were transferred to microcentrifuge tubes, excess embryo medium was removed, embryos were mixed with sample buffer (94 mM Tris pH 6.8, 3% SDS, 15% glycerol, 150 mM dithiothreitol and 0.003% bromophenol blue; 1 μ l per embryo) and lysed by vortexing and incubation at 95 °C for 10 min. Before loading, the samples were vortexed again and cleared by brief centrifugation.

The Lefty1 and H3 signals originated from different SDS–polyacrylamide gels and polyvinylidene difluoride (PVDF) membranes owing to differences in the abundance and molecular weights of these proteins. For anti-Lefty1 western blots 5, 10 or 15 embryos were loaded on 10% SDS–polyacrylamide gels (5 μ l, 10 μ l or 15 μ l, respectively). The loading of samples at the concentration used for Lefty1 blots resulted in a saturated H3 signal; thus, samples were diluted fivefold to quantify H3 levels using 12% SDS–polyacrylamide gels. To resolve Lefty1 well and separate it from unspecific bands, we let proteins with a molecular weight of less than 25 kDa run off the gels for Lefty1 immunoblots, making subsequent detection of H3 (~15 kDa) impossible.

Proteins were blotted onto PVDF membranes using the Trans-Blot Turbo Transfer System (Bio-Rad) in ‘mixed molecular weight’ mode. Blotted membranes were blocked in PBST containing 5% milk powder for 1 h at room temperature and incubated with the primary antibody (diluted in PBST containing 5% milk powder; 1:2,000 for the Lefty1 antibody³⁵ and 1:10,000 for the histone H3 antibody (ab1791, Abcam)) at 4°C overnight. The membranes were briefly rinsed with PBST, washed twice with PBST for 5 min and washed two more times with PBST for 10 min at room temperature. Membranes were then incubated with HRP-coupled anti-rabbit antibody (111-035-003, Jackson ImmunoResearch; diluted 1:10,000 in PBST containing 5% milk powder) for 1.5 h at room temperature, followed by a brief rinse with PBST, two washes with PBST for 5 min and two washes for 10 min at room temperature. Fresh PBST was added to the membranes before application of SuperSignal West Dura Extended Duration Substrate (Thermo Fisher Scientific). Chemiluminescence was detected with a Fusion Solo imaging system (Vilber Lourmat).

TIFF images were analysed in Fiji. Regions of interest were drawn around Lefty1 or H3 bands and the mean intensity values were used for further analysis. For lanes without clear Lefty1 bands, the signal intensity was measured at the position of the expected molecular weight based on embryos overexpressing *squint*. The region of interest dimensions were constant for all lanes measured on a given membrane (Supplementary Fig. 8). We did not subtract background intensities for the quantifications in Supplementary Fig. 5, which seemed to be higher in untreated than in extirpated embryos (Supplementary Fig. 8), although single bands in the untreated or extirpated samples did not consistently follow this general trend (perhaps representing yolk proteins⁶⁵ and possibly reflecting sample-related differences in de-yolking efficiency). The Lefty1 signal from samples with 10 embryos provided the most reliable signal, whereas the signal for samples with 5 embryos was not robustly detectable and the signal from samples with 15 embryos might be close to saturation (Supplementary Fig. 5c).

Injection of *lft1-GFP* mRNA into the YSL. mRNA encoding Lefty1-GFP³³ was generated by plasmid linearization with NotI-HF (NEB), purification with a Qiagen PCR clean-up kit and in vitro transcription using SP6 mMessage mMachine kits (Ambion). To mimic endogenous Lefty secretion, a physiologically relevant amount of 100 pg *lft1-GFP* mRNA was precisely injected into 4 hpf (the sphere stage) pronase-dechorionated embryos at two equidistant points (1 nl of 50 ng μ l⁻¹ *lft1-GFP* mRNA per point) within the embryonic YSL. To identify physiologically relevant amounts, 40, 60, 80, 100, 160 and 200 pg *lft1-GFP* mRNA were tested in a careful titration series, and 100 pg *lft1-GFP* mRNA were found to most efficiently rescue *lft1*^{-/-};*lft2*^{-/-} mutants.

Extirpations were performed 20–30 min after YSL injections. Embryos were divided into three groups: one group was fixed at the shield stage and processed for FISH, the second was incubated in embryo medium at 28°C in 24-well plates covered with 2% agarose (1 embryo per well) for phenotypic analysis at 24 hpf, and the third group was processed for imaging 45–60 min after YSL injections. Mounting for imaging was done as described above for FISH samples. Movies were recorded with identical imaging conditions. Embryos were imaged for a total of approximately 100 min and Fiji was used to generate the movies. For measurements of Lefty1-GFP intensity, injections of *lft1-GFP* mRNA in the YSL and extirpations were performed as described above, but imaging was carried out 1.5–2 h after injection. Samples were captured with identical imaging conditions. Twenty confocal slices were used for z-projections over a depth of 53 μ m, and the intensity of equivalent areas of the images was quantified using the ‘measure’ plug-in in Fiji.

Hindering Lefty1-GFP diffusion. The morphotrap construct⁴⁰ comprises a strong GFP binder (K_d : ~0.3 nM)⁶⁶. The morphotrap construct was digested with *Xho*I and *Xba*I to insert the morphotrap into a pCS2+ expression plasmid. mRNA was generated as described above for *lft1-GFP*. One nanolitre containing 100–150 pg mRNA encoding the morphotrap was injected into one-cell-stage embryos for experiments shown in the middle panel of Supplementary Fig. 4e. Transplantation of cells expressing the morphotrap (bottom panel of Supplementary Fig. 4e) was performed as described above for the extirpation experiments. Briefly, 50–100 cells were transplanted from a sphere-stage donor previously injected with 200 pg morphotrap-encoding mRNA into the sphere-stage host embryos previously injected with 50 pg *lft1-GFP* mRNA.

Time-lapse imaging experiments (Supplementary Videos 2 and 3) showed that Lefty1-GFP mobility from the YSL is strongly affected by the presence of the morphotrap. However, Lefty1-GFP mobility is not abolished entirely. This outcome is expected—even for a high-affinity GFP binder—if binding is reversible and the on/off kinetics are fast³⁹. The strong membrane localization of Lefty1-GFP in

embryos expressing the morphotrap confirmed the high affinity. The movement of the Lefty1-GFP signal appeared to follow the membranes in these embryos and is slow, consistent with a low fraction of mobile Lefty1-GFP. However, morphogenetic movements during epiboly might play an additional role in Lefty1-GFP transport, possibly facilitating Lefty spreading towards the animal pole.

Testing the effect of morphotrap binding on Lefty1-GFP activity. WT (TE) embryos were injected at the one-cell stage with 1 nl injection mix containing 5 pg or 30 pg *lft1-GFP* mRNA and 0.05% phenol red. To test the effect of the morphotrap on Lefty1-GFP activity, 150 pg *morphotrap* mRNA was included in the injection mix. Lefty overexpression phenotypes were evaluated at 24 hpf. Three groups of Nodal loss-of-function phenotypes were defined according to their strength (Supplementary Fig. 4f,g): mild (S1), intermediate (S2) and severe (S3). For imaging, embryos were mounted in 2% methylcellulose in embryo medium. Bright-field images were acquired with an Axio Zoom.V16 (Zeiss).

Lefty1-GFP gradient measurements. A physiologically relevant amount of 100 pg mRNA encoding Lefty1-GFP was injected into the YSL of *lft1*^{-/-};*lft2*^{-/-} embryos. One group of embryos was additionally injected with 150 pg *morphotrap* mRNA at the one-cell stage. Ninety minutes after YSL injections, embryos were mounted and imaged using an LSM 780 NLO (Zeiss) confocal laser scanning microscope. Embryos were imaged between 90 min and 140 min after YSL injections. To measure the gradients of secreted Lefty1-GFP from the YSL, maximum intensity projections were generated from 28 confocal slices over a depth of 194 μ m, and the ‘plot profile’ plug-in in Fiji was used to obtain the intensity of Lefty1-GFP from every point of the vegetal–animal axis in a central region of the embryo. Background values were obtained by imaging *lft1*^{-/-};*lft2*^{-/-} uninjected embryos (for the group injected with *lft1-GFP* mRNA) or *lft1*^{-/-};*lft2*^{-/-} injected with morphotrap (for the group injected with *morphotrap* + *lft1-GFP* mRNA).

Fluorescence recovery after photobleaching. WT (TE) embryos were injected at the one-cell stage with 1 nl injection mix containing 50 pg *lft1-GFP* mRNA and 0.05% phenol red. In experiments in which the effect of the morphotrap on Lefty1-GFP diffusivity was measured, 200 pg mRNA encoding the morphotrap were included in the injection mix. Pronase-dechorionated embryos were selected for homogeneous expression of the morphotrap using an Axio Zoom.V16 (Zeiss). Embryos were mounted around the oblong to the sphere stage in 1% low-melting agarose using 35-mm glass-bottom microwell dishes (MatTek). Fluorescence recovery after photobleaching (FRAP) was performed and analysed as described previously^{33,67,68} using an LSM 780 NLO (Zeiss) confocal microscope at an imaging depth of 30–40 μ m. Diffusion coefficients and production rates were fitted to the recovery curves using previously published values for Lefty1-GFP protein stability³³. The fit was constrained with a minimal diffusion coefficient of 0.1 μ m² s⁻¹, which is on the order of the speed of cell movements during early zebrafish development⁶³.

***lft1*^{-/-};*lft2*^{-/-} mutant rescue with the small-molecule Nodal inhibitor SB-505124.** Rescue experiments were performed as recently described³⁶. Extirpations were performed in 4 hpf pronase-dechorionated embryos at the sphere stage as described above. Thirty to forty minutes after extirpation, embryos were transferred to 24-well plates covered with 2% agarose (1 embryo per well) and treated with 4.8 μ M SB-505124 in embryo medium starting 40 min after extirpation (~30% epiboly stage). Embryos were then separated into two groups: one group was fixed 2–2.5 h after extirpation (the shield stage) and processed for FISH, and the second group was further incubated with the inhibitor at 28°C until 24 hpf (20 h after extirpation) for phenotypic analysis. For the experiments with increasing Nodal inhibitor exposure, different concentrations from 6 μ M to 12 μ M SB-505124 in embryo medium were tested.

Mathematical modelling. Details of the computational screen and the parameters used for modelling of the size-dependent inhibition system are described in Supplementary Note 1 and Supplementary Table 2.

Statistics and reproducibility. Two tests were performed to assess whether experimental data were normally distributed: the Kolmogorov–Smirnov ($\alpha=0.05$) and the Shapiro–Wilk tests ($\alpha=0.05$). To analyse whether experimental groups were significantly different, two-sided Student’s t-tests ($\alpha=0.05$) were performed.

Embryos from zebrafish crosses were randomly allocated into experimental groups for extirpation, injections and drug treatments. Most experiments were carried out at least twice, and the findings of all key experiments were reliably reproduced. All replicates and precise *P* values are documented in the ‘Summary’ sheet of Supplementary Table 1, which states the number of independent samples, embryos and independent experiments.

Reporting Summary. Further information on experimental design is available in the Nature Research Reporting Summary linked to this article.

Code availability. The source code for the custom scripts used for data analysis in this study is available from the corresponding author on reasonable request.

Data availability. Supplementary Table 1 contains the source data for Figs. 1a,c,d,h, 2b,c,e–i, 3a, 5c–h, 6f–j and 7e and Supplementary Figs. 2a,b, 3a–c and 4a–d. The data that support the findings of this study are available from the corresponding author on reasonable request.

References

58. Thisse, C. & Thisse, B. High-resolution in situ hybridization to whole-mount zebrafish embryos. *Nat. Protoc.* **3**, 59–69 (2008).
59. Lauter, G., Soll, I. & Hauptmann, G. Two-color fluorescent in situ hybridization in the embryonic zebrafish brain using differential detection systems. *BMC Dev. Biol.* **11**, 43 (2011).
60. Schindelin, J. et al. Fiji: an open-source platform for biological-image analysis. *Nat. Methods* **9**, 676–682 (2012).
61. Dee, C. T. et al. A change in response to BMP signalling precedes ectodermal fate choice. *Int J. Dev. Biol.* **51**, 79–84 (2007).
62. Feng, X., Adiante, E. G. & Devoto, S. H. Hedgehog acts directly on the zebrafish dermomyotome to promote myogenic differentiation. *Dev. Biol.* **300**, 736–746 (2006).
63. Pauls, S., Geldmacher-Voss, B. & Campos-Ortega, J. A. A zebrafish histone variant H2A.F/Z and a transgenic H2A.F/Z:GFP fusion protein for in vivo studies of embryonic development. *Dev. Genes Evol.* **211**, 603–610 (2001).
64. Schmid, B. et al. High-speed panoramic light-sheet microscopy reveals global endodermal cell dynamics. *Nat. Commun.* **4**, 2207 (2013).
65. Link, V., Shevchenko, A. & Heisenberg, C. P. Proteomics of early zebrafish embryos. *BMC Dev. Biol.* **6**, 1 (2006).
66. Saerens, D. et al. Identification of a universal VHH framework to graft non-canonical antigen-binding loops of camel single-domain antibodies. *J. Mol. Biol.* **352**, 597–607 (2005).
67. Pomreinke, A. P. et al. Dynamics of BMP signaling and distribution during zebrafish dorsal–ventral patterning. *eLife* **6**, e25861 (2017).
68. Blässle, A. et al. Quantitative diffusion measurements using the open-source software PyFRAP. *Nat. Commun.* **9**, 1582 (2018).

Reporting Summary

Nature Research wishes to improve the reproducibility of the work that we publish. This form provides structure for consistency and transparency in reporting. For further information on Nature Research policies, see [Authors & Referees](#) and the [Editorial Policy Checklist](#).

Statistical parameters

When statistical analyses are reported, confirm that the following items are present in the relevant location (e.g. figure legend, table legend, main text, or Methods section).

n/a | Confirmed

- The exact sample size (n) for each experimental group/condition, given as a discrete number and unit of measurement
- An indication of whether measurements were taken from distinct samples or whether the same sample was measured repeatedly
- The statistical test(s) used AND whether they are one- or two-sided
Only common tests should be described solely by name; describe more complex techniques in the Methods section.
- A description of all covariates tested
- A description of any assumptions or corrections, such as tests of normality and adjustment for multiple comparisons
- A full description of the statistics including central tendency (e.g. means) or other basic estimates (e.g. regression coefficient) AND variation (e.g. standard deviation) or associated estimates of uncertainty (e.g. confidence intervals)
- For null hypothesis testing, the test statistic (e.g. F , t , r) with confidence intervals, effect sizes, degrees of freedom and P value noted
Give P values as exact values whenever suitable.
- For Bayesian analysis, information on the choice of priors and Markov chain Monte Carlo settings
- For hierarchical and complex designs, identification of the appropriate level for tests and full reporting of outcomes
- Estimates of effect sizes (e.g. Cohen's d , Pearson's r), indicating how they were calculated
- Clearly defined error bars
State explicitly what error bars represent (e.g. SD, SE, CI)

Our web collection on [statistics for biologists](#) may be useful.

Software and code

Policy information about [availability of computer code](#)

Data collection

For data acquisition on a Lightsheet Z.1 microscope, we used ZEN 2014 SP1 Black Version 9.2.0.0 (ZEISS). For data collection on an Axio Zoom.V16 microscope, we used ZEN Blue Version 2.0.0.0 (ZEISS). For data acquisition on an LSM 780 NLO microscope, we used ZEN 2.3 SP1 Black version 14.0.0.201 (ZEISS).

Data analysis

For image analysis, we used Fiji/ImageJ version 1.51. 2D maps were re-aligned using the Hugin panorama photo stitcher software 2016.0.0. Most simulations were executed in Python 2.7.8 with scipy 0.19.0, numpy 1.14.0, fipy 3.1, and matplotlib 1.5.3. Simulations in Fig. 7a,b were performed in COMOL Multiphysics version 3.5a. FRAP data was analysed using MATLAB 7.10.0 (R2010a), COMSOL Multiphysics version 3.5a, and custom scripts. The source code for custom scripts used for data analysis in this study is available from the corresponding author.

For manuscripts utilizing custom algorithms or software that are central to the research but not yet described in published literature, software must be made available to editors/reviewers upon request. We strongly encourage code deposition in a community repository (e.g. GitHub). See the Nature Research [guidelines for submitting code & software](#) for further information.

Data

Policy information about [availability of data](#)

All manuscripts must include a [data availability statement](#). This statement should provide the following information, where applicable:

- Accession codes, unique identifiers, or web links for publicly available datasets
- A list of figures that have associated raw data
- A description of any restrictions on data availability

The data that support the findings of this study are available from the corresponding author.

Field-specific reporting

Please select the best fit for your research. If you are not sure, read the appropriate sections before making your selection.

Life sciences Behavioural & social sciences Ecological, evolutionary & environmental sciences

For a reference copy of the document with all sections, see [nature.com/authors/policies/ReportingSummary-flat.pdf](https://www.nature.com/authors/policies/ReportingSummary-flat.pdf)

Life sciences study design

All studies must disclose on these points even when the disclosure is negative.

Sample size	At least three biological replicates were estimated to provide an adequate sample size based on previous analyses (Müller et al., Science 2012; Müller et al., Development 2013, Pomreinke et al., eLife 2017). For most experiments, we exceeded this minimal sample size to reduce the relative standard error.
Data exclusions	Data was excluded using pre-established criteria. To assess the survival of extirpated embryos without considering other mechanical disruptions of the extirpation assay (such as wound healing failure or mechanical constraints due to changes in the embryo/yolk ratio), embryos that did not survive extirpation or that did not proceed to gastrulation were discarded. For FRAP experiments, we discarded embryos with a non-uniform distribution of Lefty1-GFP since the model to fit the data assumes a uniform fluorescence distribution around the bleached domain.
Replication	Most experiments were carried out at least twice, and the experimental findings were reliably reproduced.
Randomization	Embryos from zebrafish crosses were randomly allocated into experimental groups for extirpation, injections, and drug treatments.
Blinding	Since embryos from zebrafish crosses were genetically uniform and indistinguishable, blinding of the investigators was not necessary.

Reporting for specific materials, systems and methods

Materials & experimental systems

n/a	Involvement in the study
<input type="checkbox"/>	<input checked="" type="checkbox"/> Unique biological materials
<input type="checkbox"/>	<input checked="" type="checkbox"/> Antibodies
<input checked="" type="checkbox"/>	<input type="checkbox"/> Eukaryotic cell lines
<input checked="" type="checkbox"/>	<input type="checkbox"/> Palaeontology
<input type="checkbox"/>	<input checked="" type="checkbox"/> Animals and other organisms
<input checked="" type="checkbox"/>	<input type="checkbox"/> Human research participants

Methods

n/a	Involvement in the study
<input checked="" type="checkbox"/>	<input type="checkbox"/> ChIP-seq
<input checked="" type="checkbox"/>	<input type="checkbox"/> Flow cytometry
<input checked="" type="checkbox"/>	<input type="checkbox"/> MRI-based neuroimaging

Unique biological materials

Policy information about [availability of materials](#)

Obtaining unique materials There are no restrictions on the availability of materials, which can be obtained from standard commercial sources or from the corresponding author. The only exception is the antibody directed against zebrafish Lefty1, which was obtained from Dr. Caroline Hill (The Francis Crick Institute).

Antibodies

Antibodies used	We used anti-DIG-AP (Roche, 11093274910) at a dilution of 1:3000, anti-DIG-POD (Roche, 11207733910) at a dilution of 1:150, anti-DNP-POD (Perkin-Elmer, FP1129) at a dilution of 1:150, anti-phospho-Histone H3 (Cell Signaling Technologies, 3377S) at a dilution of 1:500, anti-pSmad2/3 (Cell Signaling Technologies, 8828) at a dilution of 1:2000 or 1:5000, HRP-conjugated anti-rabbit (Jackson ImmunoResearch, 111-035-003) at a dilution of 1:500, anti-Lefty1 (van Boxtel et al., Dev Cell 2015) at a dilution of 1:2000, and anti-Histone H3 (Abcam, ab1791) at a dilution of 1:10000.
Validation	We used validated primary antibodies from standard commercial sources (for validation see Moens, Cold Spring Harb Protoc 2008; Lauter et al., BMC Dev Biol 2011; Brend and Holley, JoVE 2009; van Boxtel et al., Dev Cell 2018; https://www.cellsignal.com/products/primary-antibodies/phospho-histone-h3-ser10-d2c8-xp-rabbit-mab/3377 ; https://www.cellsignal.com/products/primary-antibodies/phospho-smad2-ser465-467-smad3-ser423-425-d27f4-rabbit-mab/8828 ; Vastenhouw et al., Nature 2010). The only exception is the antibody directed against zebrafish Lefty1, which was validated by Dr. Caroline Hill's laboratory (The Francis Crick Institute) in van Boxtel et al., Dev Cell 2015. We also validated the specificity of this antibody by generating "negative control" embryos treated with the Nodal inhibitor SB-505124 (which inhibits lefty1 expression) and "positive control" embryos injected with Squint-encoding mRNA (which induces endogenous lefty1 expression).

Animals and other organisms

Policy information about [studies involving animals](#); [ARRIVE guidelines](#) recommended for reporting animal research

Laboratory animals	All procedures involving animals were executed in accordance with the guidelines of the State of Baden-Württemberg (Germany) and approved by the Regierungspräsidium Tübingen (35/9185.46-5, 35/9185.81-5). We performed experiments exclusively on zebrafish embryos and larvae that were at most two days old and were not yet freely feeding. We used wild type (TE and TLAB strains) and Lefty mutant zebrafish embryos generated by TALEN-mediated targeted mutagenesis (Rogers et al., eLife 2017).
Wild animals	We did not use wild animals.
Field-collected samples	We did not use field-collected samples.